

**RESEARCH ARTICLE**

# Parametric model order reduction and its application to inverse analysis of large nonlinear coupled cardiac problems

M. R. Pfaller\*<sup>1</sup> | M. Cruz Varona<sup>2</sup> | J. Lang<sup>1</sup> | C. Bertoglio<sup>3</sup> | W. A. Wall<sup>1</sup>

<sup>1</sup>Institute for Computational Mechanics,  
Technical University of Munich,  
Boltzmannstr. 15, 85748 Garching b.  
München, Germany

<sup>2</sup>Chair of Automatic Control,  
Technical University of Munich,  
Boltzmannstr. 15, 85748 Garching b.  
München, Germany

<sup>3</sup>Bernoulli Institute, University of  
Groningen, Nijenborgh 9, 9747 AG  
Groningen, The Netherlands

**Correspondence**

\*M. R. Pfaller, Boltzmannstr. 15,  
85748 Garching b. München, Germany.  
Email: martin.pfaller@tum.de

**Abstract**

Predictive high-fidelity finite element simulations of human cardiac mechanics commonly require a large number of structural degrees of freedom. Additionally, these models are often coupled with lumped-parameter models of hemodynamics. High computational demands, however, slow down model calibration and therefore limit the use of cardiac simulations in clinical practice. As cardiac models rely on several patient-specific parameters, just one solution corresponding to one specific parameter set does not at all meet clinical demands. Moreover, while solving the nonlinear problem, 90% of the computation time is spent solving linear systems of equations. We propose a novel approach to reduce only the structural dimension of the monolithically coupled structure-windkessel system by projection onto a lower-dimensional subspace. We obtain a good approximation of the displacement field as well as of key scalar cardiac outputs even with very few reduced degrees of freedom, while achieving considerable speedups. For subspace generation, we use proper orthogonal decomposition of displacement snapshots. To incorporate changes in the parameter set into our reduced order model, we provide a comparison of subspace interpolation methods. We further show how projection-based model order reduction can be easily integrated into a gradient-based optimization and demonstrate its performance in a real-world multivariate inverse analysis scenario. Using the presented projection-based model order reduction approach can significantly speed up model personalization and could be used for many-query tasks in a clinical setting.

**KEYWORDS:**

Cardiac mechanics, parametric model order reduction, proper orthogonal decomposition, inverse analysis

arXiv:1810.12033v1 [cs.CE] 29 Oct 2018

## 1 | INTRODUCTION

Cardiac solid mechanics simulations consist of solving large-deformation, materially nonlinear, elastodynamic coupled boundary-value problems. As the exact fluid dynamics of blood within the heart are usually not needed, the structural model is commonly coupled to lumped-parameter fluid models which provide the pressure to the endocardial wall<sup>1</sup>. These so-called windkessel models are then coupled to cardiac solid mechanics<sup>2</sup>. For a comprehensive review of models currently utilized in cardiac mechanics the reader is referred to<sup>3</sup>.

## 1.1 | Model order reduction

The needed huge number of degrees of freedom (*DOFs*) and other challenges of solving coupled nonlinear problems make the solution of cardiac models computationally expensive and limit the models' use in clinical practice. For example, using a single node with 24 cores, a simulation of one heartbeat, which takes about one second in reality, takes about one day to compute with our high-fidelity four chamber model<sup>4</sup>. The potential to reduce computation time motivates the use of reduced order models (*ROMs*). In the following, different strategies in reduced order modeling are reviewed.

An important category of cardiac *ROMs* are "bottom up" *ROMs*. For these models, the same system of differential equations as for the full order model (*FOM*) is solved, but on a simplified analytical geometry. The displacements are commonly parameterized by only one scalar degree of freedom (*DOF*). These models are thus referred to as 0D models. Examples in this category include monoventricular cylindrical<sup>5</sup>, spherical<sup>6</sup>, or prolate spheroid<sup>7</sup> or biventricular<sup>8</sup> geometries. These models allow extremely fast evaluation, with computation times less than one second. Their results are, however, only lumped quantities which usually need an extra correction step in order to predict the solution of a corresponding patient-specific 3D model.

Another approach of *MOR* in biomechanics is the use of coarsely discretized geometries, see e.g.<sup>9,10</sup>. Coarsely discretized models are easy to implement, since the computational framework is identical to the one of the *FOM*. The disadvantage of using coarsely discretized geometries is that there is no exact control over the approximation quality and important features of the *FOM* might not be preserved by the *ROM*.

A third category of cardiac *ROMs* are "top down" *ROMs*, which are utilized in this work. These *ROMs* make a model computationally less expensive by reducing the dimension of the problem, starting from the *FOM*. For example in cardiac electrophysiology, approximated lax pairs for propagating wave fronts were proposed in<sup>11,12</sup>. A local reduced basis method for parameterized cardiac electrophysiology was recently introduced in<sup>13</sup>. Reduced basis methods were proposed for general large deformation, material nonlinear finite element simulations<sup>14,15</sup>. A framework for linear coupled multiphysics problems was introduced in<sup>16</sup>.

For large-scale finite element simulation, about 90 % of the time is spent iteratively solving linear systems of equations. This proportion motivates the use of model order reduction by projection, where the full linear system is projected onto a much smaller dimensional subspace while preserving the model's most relevant features. The solution of the *FOM* is then approximated by a solution in the reduced space with a *ROM*. A popular method to generate such subspaces is proper orthogonal decomposition (*POD*), which is purely observation-based and independent of the underlying physics of the model. The snapshots, in our case transient observations of displacements, can be obtained from a *FOM* simulation of one heartbeat.

There are only few examples where *POD* has been applied to cardiac problems. The reduction of a patient-specific biventricular cardiac model using *POD* is described in<sup>17</sup>. A quasi-static cardiac model was reduced using *POD* in<sup>18</sup> and combined with hyperreduction techniques. However, analysis was only carried out using an idealized ellipsoidal left ventricular geometry with few *DOFs*. While this is very instructive, results for speedup and accuracy of the *ROM* are not conclusive for real-world cardiac problems. Furthermore, both references used a purely structural cardiac model with prescribed blood pressures.

Cardiac models rely on a large set of patient-specific parameters, describing constitutive behavior, hemodynamics, boundary conditions, or local fiber orientation. In order not to rely on a *FOM* simulation for each new *ROM* simulation, which would render the *ROM* simulation useless, the reduced subspace must be able to adapt to a changing parameter set. This adaptation requires parametric model order reduction (*pMOR*). Among many global and local *pMOR* techniques, various subspace interpolation methods have been proposed in the past<sup>19</sup>. Specifically, a popular method using a Grassmann manifold was proposed in<sup>20</sup> and illustrated with a large coupled aeroelastic model of a fighter jet. The method proposed in<sup>17</sup> uses direct interpolation of parameter-dependent solutions instead of interpolating subspaces. Furthermore, a global *pMOR* approach using a global basis over the whole parameter range is employed in<sup>18</sup>.

The performance of *POD* in realistic coupled simulations of cardiac contraction is yet unknown. We demonstrate in this work the performance of *POD* applied to a patient-specific cardiac geometry with about 850 000 structural *DOFs*. To the best of the authors' knowledge, *POD* for large nonlinear models has only been applied to single fields, e.g. structural mechanics or fluid dynamics, separately<sup>21</sup>. In this work, we consider for the first time the case of a *POD*-reduced 3D structural model that is monolithically coupled to a 0D windkessel model, where we only reduce the structural dimension of the problem. Additionally, we compare several subspace interpolation methods for cardiac contraction. In these parametric simulations, we vary the contractility parameter controlling maximum active tension of the myofibers in our model, as it is the most influential parameter for cardiac function and commonly calibrated to experiments.

## 1.2 | Inverse analysis

Many of the cardiac model parameters depend on a patient's physiology and are *a priori* unknown, as invasive experiments cannot be carried out on living human subjects. A predictive patient-specific cardiac model is thus subject to an iterative process termed *inverse analysis*. In this context, the simulation of one heartbeat with given parameters can be regarded as the forward problem. The reverted task of matching the parameters to given observations from the patient-specific heartbeat is then the inverse problem. Common clinical measurements of cardiac kinematics are displacement data extracted from cine or tagged magnetic resonance imaging (MRI), representing an Eulerian and Lagrangian description of motion, respectively. Other measurements include blood pressure or electrocardiograms. As cardiac mechanics simulations pose an expensive forward problem, repeated evaluation during inverse analysis has incredible computational demands. Furthermore, algorithms for inverse analysis commonly scale linearly with the number of parameters. Inverse analysis is thus a promising application of reduced order modeling.

During gradient-based optimization, the adjoint method offers computationally inexpensive gradient calculation. For example in<sup>22</sup>, regional contractility was estimated from short axis cine MRI. Using the adjoint method, ischemic regions in cardiac electrophysiology were identified in<sup>23</sup>. Most recently in<sup>24</sup>, passive material parameters and active fiber shortening was estimated for a biventricular geometry from ventricular volume and regional strain.

Gradient-free inverse analysis for cardiac problems was demonstrated in<sup>25</sup>, where regional cardiac contractility was estimated from cine MRI using the unscented Kalman filter (UKF). The reduced order UKF was further applied in<sup>26,27</sup> to estimate boundary condition parameters of the aorta for a fluid-structure-interaction problem. Other examples of gradient-free inverse analysis include<sup>28</sup>, where left-ventricular active and passive material parameters were estimated from 3D tagged MRI using a parameter sweep.

There are some examples, where reduced order modeling has been combined with inverse analysis in biomechanics. For arterial hemodynamic fluid-structure-interaction problems, an inverse analysis with uncertainty quantification was performed in<sup>29</sup> using a reduced basis method. There are however few references for cardiac solid models. In<sup>17</sup>, the reduced order UKF was applied to estimate cardiac contractility in a healthy and an infarcted region. The forward simulations were carried out using *POD*, thus converging to a different solution than using the *FOM* only. In<sup>10</sup> a multifidelity approach was proposed to calibrate hemodynamical and structural parameters of a cardiac model to ventricular pressure measurements. Here, a Levenberg-Marquardt-based optimization uses evaluations switching between a 3D *FOM*, a coarsely discretized version of the 3D *FOM*, and a 2D surrogate model. Another multifidelity approach was used in<sup>30</sup> between a 3D *FOM* and a 0D surrogate model.

Using coarsely discretized or surrogate models does however not guarantee that the most important features of the *FOM* are preserved. These surrogate models further lack the ability of *pMOR* to inherently "learn" from evaluations of the *FOM* to become more precise throughout the optimization. Instead, they require an additional mapping between *FOM* and surrogate model solutions. Most importantly, using 2D or 0D surrogate models during inverse analysis, the heart can only be tuned to scalar measurements. However, a calibration to spatial measurements from cine or tagged MRI might be desired in many applications, e.g. when detecting infarcted regions<sup>25</sup>. In this work, we thus propose a novel method of how a *ROM* can be integrated into any optimization-based inverse analysis leading to considerable savings in CPU time, and demonstrate its performance in a real-world multivariate inverse analysis scenario.

The remainder of this work is structured as follows. In section 2, we introduce the full order elastodynamic and hemodynamic models. We derive a reduced formulation for the monolithically coupled system in section 3 and review several *pROM* subspace interpolation methods. In numerical experiments in section 4, we demonstrate the accuracy and speedup of our *ROM* and show its response to parametric variations. Furthermore, we propose in section 5 a *pMOR*-based method for inverse analysis and analyze its performance with our four-chamber heart model. We close with a conclusion and future perspectives in section 6.

## 2 | 3D-0D COUPLED CARDIOVASCULAR MODELING

In this section we give a brief overview of our full order model (*FOM*) which is composed of a 3D elastodynamical model, see section 2.1, coupled to a 0D hemodynamical model, see section 2.2. We further provide insights into the numerical solution of the model in section 2.3. For a more detailed description, the reader is referred to<sup>4</sup>.

## 2.1 | 3D elastodynamical model

We follow the classic approach of nonlinear large deformation continuum mechanics to model the elastodynamic problem of 3D cardiac contraction. We define the reference configuration  $\mathbf{X}$  and the current configuration  $\mathbf{x}$ , which are connected by the displacements  $\mathbf{u} = \mathbf{x} - \mathbf{X}$ . We calculate the deformation gradient  $\mathbf{F}$ , the right Cauchy-Green tensor  $\mathbf{C}$ , and the Green-Lagrange strain tensor  $\mathbf{E}$

$$\mathbf{F} = \frac{\partial \mathbf{x}}{\partial \mathbf{X}}, \quad \mathbf{C} = \mathbf{F}^T \mathbf{F}, \quad \mathbf{E} = \frac{1}{2}(\mathbf{C} - \mathbf{I}). \quad (1)$$

Balance of momentum, a Neumann windkessel coupling condition with left ventricular pressure  $p_v$ , omni-directional spring-dashpot boundary conditions, and pericardial boundary conditions yield the weak form of the 3D elastodynamic boundary value problem in the reference configuration

$$\int_{\Omega_0} [\rho_0 \ddot{\mathbf{u}} \cdot \delta \mathbf{u} + \mathbf{S} : \delta \mathbf{E}] dV + \int_{\Gamma_0^{\text{endo}}} p_v J \mathbf{F}^{-T} \cdot \mathbf{N} \cdot \delta \mathbf{u} dA + \int_{\Gamma_0^{\text{vess}}} [k_v \mathbf{u} + c_v \dot{\mathbf{u}}] \cdot \delta \mathbf{u} dA + \int_{\Gamma_0^{\text{epi}}} \mathbf{N} [k_e \mathbf{u} \cdot \mathbf{N} + c_e \dot{\mathbf{u}} \cdot \mathbf{N}] \cdot \delta \mathbf{u} dA = 0, \quad (2)$$

with density  $\rho_0$ , accelerations  $\ddot{\mathbf{u}}$ , virtual displacements and strains  $\delta \mathbf{u}$  and  $\delta \mathbf{E}$ , respectively, the Jacobian  $J = \det \mathbf{F}$  of the deformation gradient, the second Piola-Kirchhoff stress tensor  $\mathbf{S}$ , the reference surface normal  $\mathbf{N}$ , and spring stiffness  $k_v, k_e$  and viscosity  $c_v, c_e$  for vessel and epicardial surface, respectively. We define three surfaces for the imposition of boundary conditions  $\Gamma_0^{\text{endo}}$ ,  $\Gamma_0^{\text{vess}}$ , and  $\Gamma_0^{\text{epi}}$  at the left endocardium, the outside of the great vessels, and the epicardium respectively. At the cut-offs of the great vessels we apply homogeneous Dirichlet boundary conditions. We define different nonlinear materials for adipose tissue, ventricular myocardium, atria, aorta, and the pulmonary artery. The geometry and the different materials are shown in figure 1. Each is composed of a hyperelastic and a viscous contribution depending on the rate of Green-Lagrange strains. Quasi-incompressibility is enforced by a penalty potential. The ventricular myocardium is modeled with an isotropic Mooney-Rivlin material and has an additive active stress component  $\mathbf{S}_{\text{act}}$  modeling the contraction of myofiber bundles in reference fiber direction  $\mathbf{f}_0$

$$\mathbf{S}_{\text{act}} = \tau(t) \cdot \mathbf{f}_0 \otimes \mathbf{f}_0, \quad \text{with } \dot{\tau}(t) = -|u(t)|\tau(t) + \sigma|u(t)|_+, \quad \tau(0) = 0, \quad (3)$$

with active stress  $\tau \in [0, \sigma[$  and the function  $|u(t)|_+ = \max(u(t); 0)$ . The contractility parameter  $\sigma$  controls the upper limit of the active stress component. The prescribed activation function  $u(t)$  is

$$u(t) = \alpha_{\text{max}} \cdot f(t) + \alpha_{\text{min}} \cdot [1 - f(t)], \quad f(t) = S^+(t - t_{\text{sys}}) \cdot S^-(t - t_{\text{dias}}), \quad S^\pm(\Delta t) = \frac{1}{2} \left[ 1 \pm \tanh \left( \frac{\Delta t}{\gamma} \right) \right] \quad (4)$$

with steepness  $\gamma = 0.005$  s and descending and ascending sigmoid functions  $S^+$  and  $S^-$ , respectively. The indicator function  $f \in ]0, 1[$  indicates ventricular systole. The times  $t_{\text{sys}}$  and  $t_{\text{dias}}$  model the onset of systole and diastole, respectively. The times  $t_{\text{sys}}$  and  $t_{\text{dias}}$ , and maximum and minimum myocyte activation rates  $\alpha_{\text{max}}$  and  $\alpha_{\text{min}}$ , respectively, are calibrated to match the timing of ventricular systole as observed in cine MRI, as demonstrated in section 5.

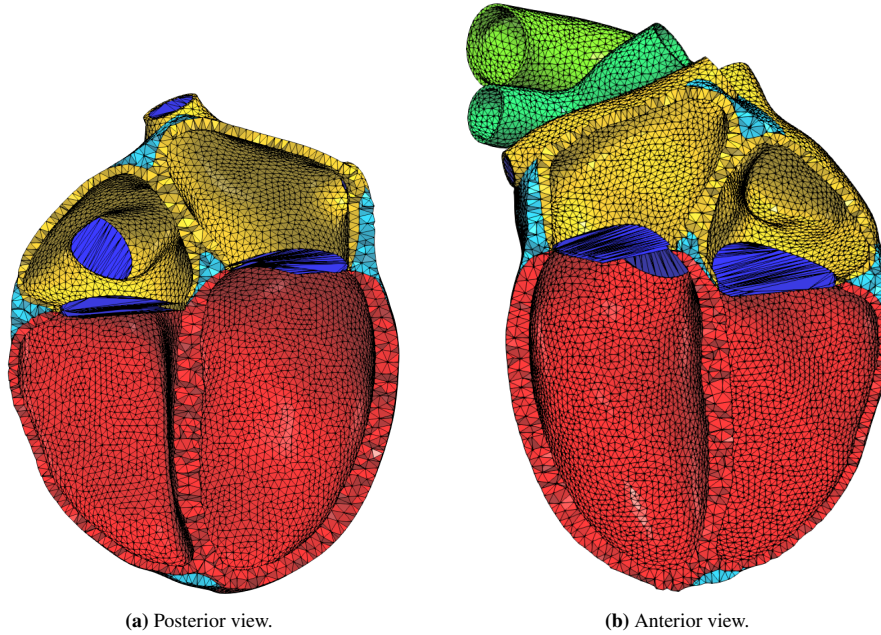
We discretize displacements  $\mathbf{u}$  and virtual displacements  $\delta \mathbf{u}$  arising in the weak form (2) using quadratic basis functions on each tetrahedral finite element. Assembly of the discretized problem leads to the matrix notation of the spatially semi-discrete residual of the full order structural model

$$\mathbf{R}_{\text{semi}}^S = \mathbf{M} \ddot{\mathbf{d}} + \mathbf{F}(\dot{\mathbf{d}}, \mathbf{d}, p_v) \stackrel{!}{=} \mathbf{0} \quad (5)$$

with mass matrix  $\mathbf{M}$ , nonlinear force vector  $\mathbf{F}$ , and nodal displacements, velocities, and accelerations  $\mathbf{d}$ ,  $\dot{\mathbf{d}}$ , and  $\ddot{\mathbf{d}}$  respectively. We discretize the boundary value problem in time using a combination of Newmark's method<sup>31</sup> and the generalized- $\alpha$  scheme<sup>32</sup> to obtain the time and space discrete structural residual  $\mathbf{R}^S(\mathbf{d}_{j+1}, p_{v,j+1})$  at time step  $j + 1$ .

## 2.2 | 0D hemodynamical model

We couple the left ventricular 3D structural model to a 0D lumped-parameter windkessel model of the circulatory system. We utilize in this work a four element windkessel, using resistances  $R$ , compliances  $C$ , and an inertance  $L_p$ . Pressures at different parts of the model are denoted by  $p_i$ . We distinguish between a proximal part  $p$  and a distal part  $d$  of the aorta. The atrial pressure  $p_{at}(t)$  is prescribed to simulate atrial systole. The venous pressure  $p_{\text{ref}}$  is kept constant. We model the atrioventricular and semilunar valves with a smooth diode-like behavior by nonlinear resistances  $R_{av} := R(p_{at}, p_v)$  and  $R_{sl} := R(p_v, p_p)$



(a) Posterior view.

(b) Anterior view.

**FIGURE 1** Computational mesh with quadratic tetrahedral elements cut in four-chamber view, colored by different materials.

respectively, depending on a sigmoid function  $R$ . This yields the set of differential equations

$$\frac{p_v - p_{at}}{R_{av}} + \frac{p_v - p_p}{R_{sl}} + \dot{V}(\mathbf{u}) = 0, \quad q_p - \frac{p_v - p_p}{R_{sl}} + C_p \dot{p}_p = 0, \quad q_p + \frac{p_d - p_p}{R_p} + \frac{L_p}{R_p} \dot{q}_p = 0, \quad \frac{p_d - p_{ref}}{R_d} - q_p + C_d \dot{p}_d = 0 \quad (6)$$

which are coupled to the 3D structural model by the ventricular pressure  $p_v$  and the change in ventricular volume  $\dot{V}$ , depending on the structural displacements  $\mathbf{u}$ . The vector of primary variables yields  $\mathbf{p} = [p_v, p_p, p_d, q_p]^T$ , including the flux  $q_p$  through the inertance  $L_p$ . We discretize the set of windkessel equations (6) in time with the one-step- $\theta$  scheme<sup>33</sup>. This yields the discrete windkessel residual  $\mathbf{R}^{OD}(\mathbf{d}_{j+1}, \mathbf{p}_{j+1})$  at time step  $j + 1$ .

### 2.3 | Solving the coupled problem

We solve the coupled 3D-0D model with the structural and windkessel residuals  $\mathbf{R}^S$  and  $\mathbf{R}^{OD}$ , respectively, for the displacements  $\mathbf{d}$  and windkessel variables  $\mathbf{p}$  at time step  $j + 1$  with the Newton-Raphson method

$$\begin{bmatrix} \frac{\partial \mathbf{R}^S}{\partial \mathbf{d}} & \frac{\partial \mathbf{R}^S}{\partial \mathbf{p}} \\ \frac{\partial \mathbf{R}^{OD}}{\partial \mathbf{d}} & \frac{\partial \mathbf{R}^{OD}}{\partial \mathbf{p}} \end{bmatrix}_{j+1}^i \cdot \begin{bmatrix} \Delta \mathbf{d} \\ \Delta \mathbf{p} \end{bmatrix}_{j+1}^{i+1} = - \begin{bmatrix} \mathbf{R}^S \\ \mathbf{R}^{OD} \end{bmatrix}_{j+1}^i, \quad (7)$$

linearizing the residuals in iteration  $i$ . The solution is converged if

$$\|\mathbf{R}^S\|_{\infty} < tol_{res}^S, \quad \|\Delta \mathbf{d}\|_{\infty} < tol_{inc}^S, \quad \|\mathbf{R}^{OD}\|_2 < tol_{res}^{OD}, \quad \|\Delta \mathbf{p}\|_2 < tol_{inc}^{OD}, \quad (8)$$

with the structural and windkessel residual and increment tolerances  $tol_{res}^S$ ,  $tol_{res}^{OD}$ ,  $tol_{inc}^S$ , and  $tol_{inc}^{OD}$ , respectively. Note that the coupled model in (7) is independent of the concrete formulation of the structural and windkessel models from sections 2.1 and 2.2 respectively. It is valid for any arbitrary residuals  $\mathbf{R}^S$  and  $\mathbf{R}^{OD}$ . For details of the model used here, again see<sup>4</sup>.

## 3 | NONLINEAR PARAMETRIC MODEL ORDER REDUCTION

The 3D-0D cardiovascular model described above represents a large-scale, nonlinear, parametrized, and monolithically coupled model, featuring multiple sources of nonlinear system behavior and depending on several model parameters. Firstly, our model

contains geometric nonlinearities, due to the use of the Green-Lagrange strain tensor  $\mathbf{E}(\mathbf{u})$ . Secondly, the utilized material laws for myocardial tissue induce material nonlinearity. The third and last source of nonlinearity is given by the nonlinear coupling between the structural and the hemodynamical model due to the Neumann windkessel boundary condition, acting in direction of the current normal vector of the endocardium. Furthermore, our model depends on many parameters  $\boldsymbol{\mu} = [\mu_1, \dots, \mu_{n_p}]^T \in \Omega \subset \mathbb{R}^{n_p}$ , classified in different categories. For instance, there exist parameters describing the constitutive behavior of the used materials (stiffness, viscosity, and incompressibility parameters), the additive active stress component  $\mathcal{S}_{\text{act}}$  (e.g. the contractility  $\sigma$ ,  $\alpha_{\text{max}}$ ,  $\alpha_{\text{min}}$ ,  $t_{\text{sys}}$ ,  $t_{\text{dias}}$ ), the hemodynamics (e.g. resistances  $R$ , compliances  $C$ , inertance  $L_p$ ), as well as the boundary conditions for the outside of the great vessels and the epicardium (spring stiffnesses  $k_v, k_e$  and dashpot viscosities  $c_v, c_e$ ). Thus, our discrete nonlinear parametrized *FOM* reads

$$\mathbf{R}(\mathbf{d}, \mathbf{p}, \boldsymbol{\mu}) = \begin{bmatrix} \mathbf{R}^S(\mathbf{d}, p_v, \boldsymbol{\mu}) \\ \mathbf{R}^{\text{OD}}(\mathbf{d}, \mathbf{p}, \boldsymbol{\mu}) \end{bmatrix}_{j+1} \stackrel{!}{=} \mathbf{0}. \quad (9)$$

The use of a 0D lumped-parameter windkessel model, instead of e.g. a 3D fluid dynamics model of the heart chambers and arteries, already simplifies the computational complexity of the coupled system. However, the numerical analysis of the present model still demands a high computational effort due to the large number of structural DOFs. While this is no problem for a few standard forward simulations, it is extremely challenging - and might even prohibit - fast model calibration, inverse analysis, and clinical applications. Therefore, our aim is to employ projection-based model order reduction to obtain a cardiovascular reduced order model (*ROM*) that accurately approximates the original model with substantially less DOFs and, consequently, less numerical effort. To this end, in section 3.1 we first apply the classical projection-based model order reduction framework to the structural component of our cardiovascular problem and further describe the numerical solution of the coupled *ROM*. A suitable strategy to compute the required projection matrix  $\mathbf{V}$  for a fixed parameter set is then explained in section 3.2. Afterwards, different subspace interpolation techniques are presented in section 3.3, in order to compute a parametric reduced order model (*pROM*) for any new parameter set. Finally, some implementation details are given in section 3.4.

### 3.1 | Cardiovascular reduced order model

As mentioned before, the high dimension of the *FOM* comes from the discretization of the 3D elastodynamical model, whereas the 0D model only contributes few, in our case four, windkessel DOFs in  $\mathbf{p}$ . Consequently, we only apply model order reduction to the structural component while the 0D hemodynamical model remains unchanged.

Our aim is to approximate the high dimensional structural solution  $\mathbf{d} \in \mathbb{R}^n$  using a linear combination of  $q \ll n$  basis vectors, with  $n$  being the number of DOFs of the full elastodynamical model. With the set of basis vectors  $\mathbf{v}_i \in \mathbb{R}^n$  contained in a projection matrix  $\mathbf{V} = [\mathbf{v}_1 \dots \mathbf{v}_q] \in \mathbb{R}^{n \times q}$  and the vector of the reduced model's DOFs  $\mathbf{d}_r \in \mathbb{R}^q$ , the approximation is

$$\mathbf{d} \approx \mathbf{V} \mathbf{d}_r. \quad (10)$$

To obtain a square system, we project the structural residual onto the space spanned by  $\mathbf{V}^T$  yielding the spatially semi-discrete reduced residual  $\mathbf{R}_{\text{semi},r}^S \in \mathbb{R}^q$

$$\mathbf{R}_{\text{semi},r}^S = \mathbf{V}^T \mathbf{R}_{\text{semi}}^S(\mathbf{V} \ddot{\mathbf{d}}_r, \mathbf{V} \dot{\mathbf{d}}_r, \mathbf{V} \mathbf{d}_r, p_v, \boldsymbol{\mu}). \quad (11)$$

This represents the Galerkin projection of the full structural residual  $\mathbf{R}_{\text{semi}}^S$  onto the subspace  $\mathcal{V}$  spanned by the vectors in  $\mathbf{V}$ . After discretization in time, we obtain the Newton-Raphson update  $i + 1$  at time step  $j + 1$  of the coupled reduced order model

$$\begin{bmatrix} \mathbf{V}^T \frac{\partial \mathbf{R}^S}{\partial \mathbf{d}} \mathbf{V} & \mathbf{V}^T \frac{\partial \mathbf{R}^S}{\partial \mathbf{p}} \\ \frac{\partial \mathbf{R}^{\text{OD}}}{\partial \mathbf{d}} \mathbf{V} & \frac{\partial \mathbf{R}^{\text{OD}}}{\partial \mathbf{p}} \end{bmatrix}_{j+1} \cdot \begin{bmatrix} \Delta \mathbf{d}_r \\ \Delta \mathbf{p} \end{bmatrix}_{j+1}^{i+1} = - \begin{bmatrix} \mathbf{V}^T \mathbf{R}^S \\ \mathbf{R}^{\text{OD}} \end{bmatrix}_{j+1}^i \quad (12)$$

by linearizing the spatially and time discrete form of the residual. Through the chain rule of differentiation, the left column entries of the block Jacobian matrix are right-multiplied by  $\mathbf{V}$ . The structural block  $\mathbf{V}^T \partial \mathbf{R}^S / \partial \mathbf{d} \mathbf{V}$  is now of reduced dimension  $\mathbb{R}^{q \times q}$ . Note that the windkessel Jacobian  $\partial \mathbf{R}^{\text{OD}} / \partial \mathbf{p}$  and windkessel degrees of freedom  $\mathbf{p}$  remain unchanged. For the off-diagonal coupling blocks  $\partial \mathbf{R}^{\text{OD}} / \partial \mathbf{d}$  and  $\partial \mathbf{R}^S / \partial \mathbf{p}$  only the structural dimension is right and left multiplied with the projection matrix  $\mathbf{V}$  or its transpose, respectively. The original (7) and reduced (12) block-Jacobian are visualized in figure 2 .

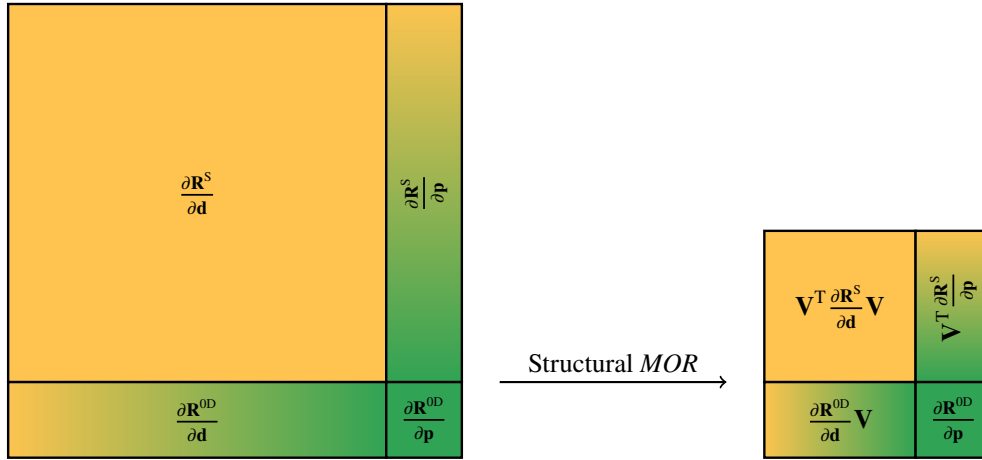


**FIGURE 2** Visualization of the Jacobian during projection-based model order reduction of the structural dimension of the block matrix system in (7) to (12). The diagonal structural and windkessel blocks are colored yellow and green, respectively. Off-diagonal coupling blocks are shaded. Note that the dimension of the diagonal windkessel block remains unchanged.

The update step of a Newton iteration is carried out by extrapolating the reduced DOFs  $\mathbf{d}_r$  to the full order displacement vector  $\mathbf{d}$  with the projection matrix  $\mathbf{V}$  by

$$\begin{bmatrix} \mathbf{d} \\ \mathbf{p} \end{bmatrix}_{j+1}^{i+1} = \begin{bmatrix} \mathbf{d} \\ \mathbf{p} \end{bmatrix}_{j+1}^i + \begin{bmatrix} \mathbf{V} \Delta \mathbf{d}_r \\ \Delta \mathbf{p} \end{bmatrix}_{j+1}^{i+1}. \quad (13)$$

Note that the full order structural residual  $\mathbf{R}^S$  and the full order block-Jacobian are always evaluated using the full order displacements  $\mathbf{d}$ . It is only after their full evaluation and assembly that their dimensions are reduced by projection. The convergence check is carried out with the reduced residual and reduced displacement increment

$$\left\| \mathbf{V}^T \mathbf{R}^S \right\|_{\infty} < \text{tol}_{\text{res}}^S, \quad \left\| \Delta \mathbf{d}_r \right\|_{\infty} < \text{tol}_{\text{inc}}^S. \quad (14)$$

The convergence criteria for the 0D windkessel model remain unchanged. As the coupled full order model (7) in section 2.3, the coupled *ROM* in (12) is valid for any full order structural and windkessel residual  $\mathbf{R}^S$  and  $\mathbf{R}^{OD}$ , respectively.

### 3.2 | Subspace computation via POD

In this work, we use the method of Proper Orthogonal Decomposition (*POD*) to compute the reduced basis  $\mathbf{V}$  required for the projection-based reduction of our full problem. *POD*<sup>34,35</sup> is a straightforward and very well-known nonlinear model reduction approach, which relies on so-called *snapshots*, i.e. discrete-time observations of the solution of our *FOM* for a fixed parameter set  $\boldsymbol{\mu}$ , to construct the basis  $\mathbf{V}$ . Given  $n_s \ll n$  snapshots  $\mathbf{d}_i$  gained from a numerical simulation of the *FOM* sample point, we obtain the snapshot matrix

$$\mathbf{D} = [\mathbf{d}_1, \dots, \mathbf{d}_{n_s}] \in \mathbb{R}^{n \times n_s}. \quad (15)$$

The goal of *POD* is to construct a basis for an optimal approximation of the *solution manifold* spanned by the snapshot matrix. In other words, the aim is to generate a basis that optimally approximates the information gathered in the snapshots. Therefore, we perform a singular value decomposition (SVD) of the snapshot matrix

$$\mathbf{D} = \mathbf{U} \boldsymbol{\Sigma} \mathbf{T}^T \quad (16)$$

with the orthogonal matrices  $\mathbf{U} \in \mathbb{R}^{n \times n}$  and  $\mathbf{T} \in \mathbb{R}^{n_s \times n_s}$  containing the left and right singular vectors, respectively, stored column-wise. The diagonal matrix

$$\boldsymbol{\Sigma} = \text{diag}(\sigma_1, \dots, \sigma_{n_s}) \in \mathbb{R}^{n \times n_s}, \quad \text{where } \sigma_1 \geq \dots \geq \sigma_{n_s} \geq 0, \quad (17)$$

features all  $n_s$  singular values  $\sigma_i$  sorted in descending order on its main diagonal. We now select the first  $q$  singular vectors  $\mathbf{u}_i$  from the columns of the left singular matrix  $\mathbf{U}$  corresponding to the  $q$  largest singular values  $\sigma_i$  in  $\mathbf{\Sigma}$  to obtain the basis vectors

$$\mathbf{v}_i = \mathbf{u}_i, \quad \forall i \in \{1, \dots, q\} \quad (18)$$

of the projection matrix  $\mathbf{V}$ . The singular values  $\sigma_i$  are frequently used to define the Relative Information Content (RIC)

$$RIC(q) = \frac{\sum_{i=1}^q \sigma_i^2}{\sum_{i=1}^{n_s} \sigma_i^2} \in [0, 1]. \quad (19)$$

This measure allows to select an appropriate basis dimension  $q$  such that  $RIC(q) \geq 1 - \varepsilon_{\text{POD}}$  for a given small tolerance  $\varepsilon_{\text{POD}}$ .<sup>18</sup> The approximation error made by selecting  $q < n_s$  basis vectors can be quantified by the sum of the squared truncated singular values

$$e(q) = \sum_{i=q+1}^{n_s} \sigma_i^2. \quad (20)$$

Note that this technique provides an optimal basis for the approximation of the snapshot matrix in a least-squares sense.<sup>36,37,38</sup> Thus, the efficiency of *POD* and the basis quality crucially depends on the selection of snapshots, which is required to represent the model's dynamics behavior sufficiently. Further note that *POD* requires the expensive numerical simulation of the full forward model, in general for many parameter sets, to collect representative snapshots. Nevertheless, this data-driven approach is very well applicable for the reduction of any nonlinear system.

### 3.3 | Interpolation of subspaces

The cardiac model described in section 2 relies on many patient-specific parameters, describing e.g. constitutive behavior, hemodynamics, boundary conditions, or local fiber orientation. Consequently, a repeated model evaluation and simulation for many different values of the parameters is indispensable to personalize the model. The aim of parametric model order reduction (*pMOR*) is to find a reduced cardiovascular model that preserves the parameter-dependency, thus allowing a variation of any of the parameters directly in the reduced model without having to repeat the whole reduction process each time. The parametric reduced model can be then used e.g. for patient-specific parameter estimation or uncertainty quantification purposes.

To efficiently reduce the parametric cardiovascular model, we decompose the *pMOR* procedure into an offline and online stage. In the *offline phase*, the parametrized full order model with  $n_p$  parameters  $\boldsymbol{\mu} = [\mu_1, \dots, \mu_{n_p}]^T \in \mathbb{R}^{n_p}$  is first simulated for several parameter sample points  $\boldsymbol{\mu}_k, k = 1, \dots, K$ , and then corresponding local projection bases  $\mathbf{V}(\boldsymbol{\mu}_k)$  are computed via *POD* from the data obtained. In the *online phase*, the projection matrix  $\mathbf{V}(\boldsymbol{\mu}^*)$  for a new parameter value  $\boldsymbol{\mu}^*$  is generated by interpolating between the precomputed subspaces.

In this paper, different subspace interpolation techniques are examined, which will be explained in the following. To do so, we suppose that local basis matrices  $\mathbf{V}_1 = \mathbf{V}(\boldsymbol{\mu}_1), \dots, \mathbf{V}_K = \mathbf{V}(\boldsymbol{\mu}_K) \in \mathbb{R}^{n \times q}$  spanning the subspaces  $\mathcal{V}(\boldsymbol{\mu}_1), \dots, \mathcal{V}(\boldsymbol{\mu}_K)$  have been computed in the offline phase from the snapshot matrices  $\mathbf{D}(\boldsymbol{\mu}_1), \dots, \mathbf{D}(\boldsymbol{\mu}_K) \in \mathbb{R}^{n \times n_s}$  at the sample points  $\boldsymbol{\mu}_1, \dots, \boldsymbol{\mu}_K$ . Each basis matrix  $\mathbf{V}(\boldsymbol{\mu}_k)$  is composed of the vectors  $\{\mathbf{v}_i(\boldsymbol{\mu}_k)\}_{i=1}^q$ . For the interpolation, appropriate weighting functions  $w_k(\boldsymbol{\mu}^*)$  should be selected to compute the interpolated basis  $\mathbf{V}(\boldsymbol{\mu}^*)$  in the online phase. Basically, any multivariate interpolation method could be used for this purpose: e.g. polynomial interpolation (Lagrange polynomials), piecewise polynomial interpolation (splines), radial basis functions (RBF), Kriging interpolation (Gaussian regression), inverse distance weighting (IDW) based on nearest-neighbor interpolation or even sparse grid interpolation.<sup>19</sup> For simplicity, in this paper we consider the special case of piecewise linear interpolation. We compare in this work four interpolation methods: weighted concatenation of bases, weighted concatenation of snapshots, adjusted direct basis interpolation, and basis interpolation on a Grassman manifold. A detailed mathematical description of the subspace interpolation methods is given in appendix A.

### 3.4 | Implementation details

The coupled *FOM* and *ROM* in (7) and (12), respectively, are solved using our in-house parallel high-performance finite element software package BACI<sup>39</sup>. The code is implemented in C++ making use of the Trilinos library<sup>40</sup>. To solve *FOM*'s large linear system in (7) we use a parallel iterative GMRES solver with  $2 \times 2$  block SIMPLE-like preconditioning. For the *ROM*'s



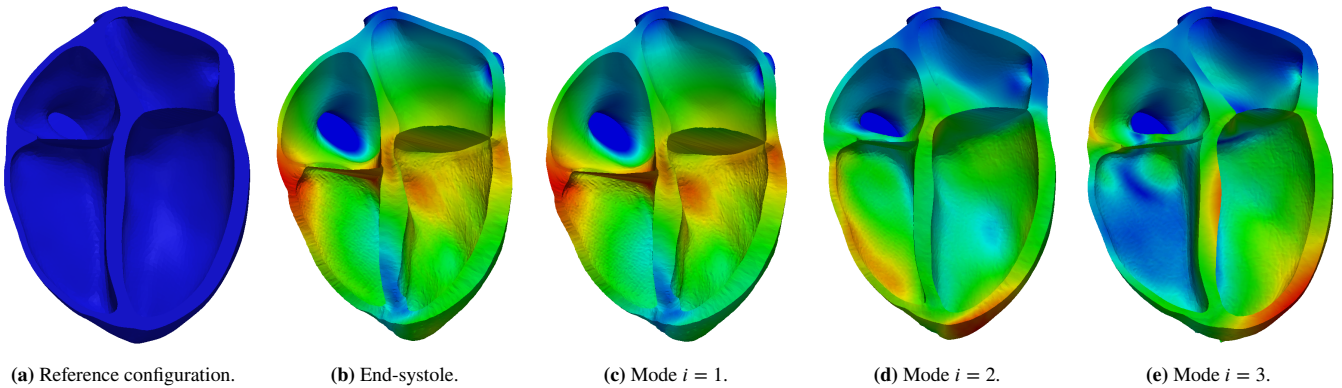


**FIGURE 3** Visualized displacements in four-chamber-view. Displacements increase from blue to red regions.

small linear system in (12) we use a serial direct solver. All preliminary calculations, i.e. singular value decompositions and the interpolation of subspaces, are performed in MATLAB (Release 2017b, The MathWorks, Inc., Natick, MA, USA).

## 4 | NUMERICAL RESULTS AND DISCUSSION

In this section we present results for the approximation of the *FOM* simulation with *ROM* simulations. We distinguish here between model order reduction and parametric model order reduction. For a fixed parameter set, using the contractility  $\sigma = 280$  kPa, we explore the approximation qualities of *POD* in section 4.1. Afterwards, we analyze the approximation quality with respect to a changing contractility in section 4.2. We employ a four chamber geometry obtained in vivo from a 33 year old healthy female volunteer. The imaging data was acquired at King’s College London, UK using a Philips Achieva 1.5T magnetic resonance imaging (MRI) scanner. The geometry was meshed using Gmsh<sup>41</sup> with a resolution of 2 mm, yielding 282 288 nodes and 167 232 quadratic tetrahedral elements, totalling  $n = 846\,864$  structural degrees of freedom (DOFs). Additionally, we have four windkessel DOFs. The cut geometry is displayed in figure 3 a.

### 4.1 | Model order reduction

In this section we demonstrate the reducibility of our coupled hemodynamical-structural simulation model of a cardiac cycle and compare computational costs. Following analysis of the heart’s eigenmodes in section 4.1.1, we investigate the approximation quality of *POD* using a varying number of modes  $q \in \{10, 50, 100, 200, 300, 400, 500\}$  in section 4.1.2. The model *ROM10* was the model with the smallest mode number, where the cardiac simulation converged to a result in all time steps. The highest mode number for *ROM500* was chosen, since there is a plateau around  $q = 500$  in the decay of singular values in figure 4 a. We further demonstrate the computational speedup achieved by using *POD* in section 4.1.3 using again varying mode numbers.

#### 4.1.1 | POD-modes of the heart

To study the reducibility of our cardiac model, we analyze the decay of the singular values compared to the first one. This gives a measure of relative importance of the modes selected by *POD*. In figure 4 a we show the normalized singular value  $\sigma_i/\sigma_1$  of mode  $i$ . For modes  $i < 50$  there is a fast decay in relative importance, indicating good reducibility. There is a plateau for  $250 < i < 700$ , indicating that not much new information is gained by including those modes in the *ROM*.

The first modes of the heart are visualized in figure 3 , where the heart is cut in four-chamber-view. The simulation in reference configuration and at end-systole are shown in figures 3 a and 3 b, respectively. Mode  $i = 1$  in figure 3 c exhibits great similarity to the solution at end-systole and is characterized by a movement of the atrioventricular plane towards the apex with negligible change in outer shape of the heart. Mode  $i = 2$  in figure 3 d consists of a more radial displacement of the outer walls of the ventricles and a pendulum motion of the intraventricular septum. Mode  $i = 3$  in figure 3 e displays a rotating motion of the ventricles together with a large left-to-right movement of the intraventricular septum.

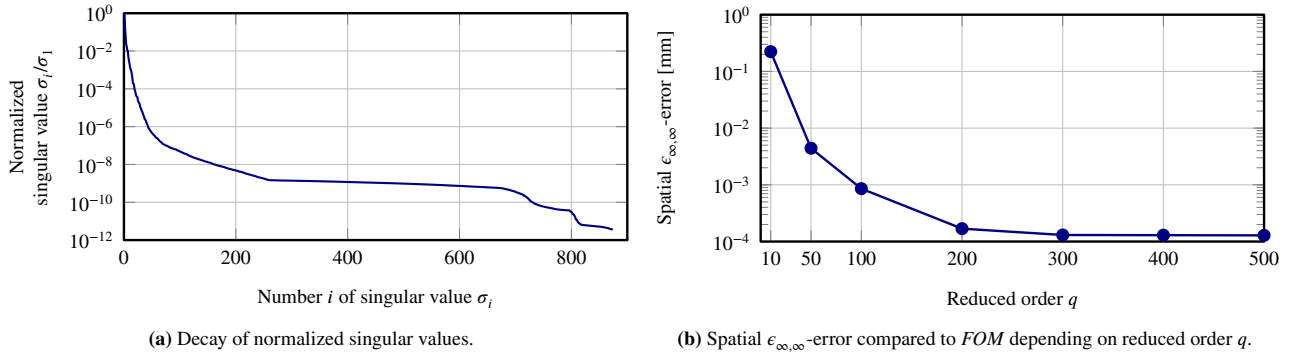


FIGURE 4 Accuracy of ROM.

### 4.1.2 | Approximation quality

To quantify the overall approximation quality of *ROM* simulations, we calculate a spatial error compared to the *FOM* solution. We define here the spatial  $\epsilon_{\infty, \infty}$ -error

$$\epsilon_{\infty, \infty} = \max_{t_j} \left[ \max_k \left\| \mathbf{d}_{\text{ROM}}^k(t_j) - \mathbf{d}_{\text{FOM}}^k(t_j) \right\| \right] \quad (21)$$

with  $\mathbf{d}_{\text{ROM}}^k(t_j)$  and  $\mathbf{d}_{\text{FOM}}^k(t_j)$  as nodal displacements at node  $k$  at time step  $t_j$  of *ROM* and *FOM* respectively. The spatial  $\epsilon_{\infty, \infty}$ -error thus gives the highest displacement error at any node at any time step and is an upper bound for all spatial approximation errors. The  $\epsilon_{\infty, \infty}$ -error is shown in figure 4 b depending on the number of reduced modes  $q$ . It is clearly evident that the approximation error strongly decreases, when more modes are used for the approximation. Remarkably, even for the very low number of 10 modes we obtain a solution whose largest approximation error at any node at any time step is below 1 mm, which is the order of magnitude of our MRI resolution from which the geometry was obtained. Furthermore, using *ROM* simulations with a reduced order of  $q > 300$  does not yield significant improvements in terms of accuracy. This is in agreement with the decay of the normalized singular values in figure 4 a, where modes  $q > 300$  contain little more information than the preceding ones.

For many medical applications, it is not necessary to calculate an accurate spatial displacement field. There are rather a couple of scalar quantities which are used in clinical practice, e.g. as a cardiac performance indicator or for the prediction of disease progression. Such a quantity is the ejection fraction

$$\text{EF} = \frac{\max V - \min V}{\max V}, \quad (22)$$

which is calculated from left or right ventricular volume. To evaluate the approximation of the EF by a *ROM* simulation, we compare in figure 5 a the left ventricular (LV) volume curves of the *FOM* simulation with *ROM* simulations of various reduced orders  $q$ . It shows that minimum and maximum volume are approximated well and the time curves are almost indistinguishable. We further compare left ventricular pressure over time for all simulations in figure 5 b. Again, key features such as maximum pressure are approximated well. Minor oscillations occur for *ROM10* and *ROM50* after the closure of the mitral valve at  $t \approx 0.2$ . Furthermore, the closure of the aortic valve at  $t \approx 0.5$  is delayed slightly for simulation *ROM10*.

### 4.1.3 | Speedup

For performance measurements, we ran all *FOM* and *ROM* simulations on a single node of our Linux cluster. One node features 64 GB of RAM and two Intel Xeon E5-2680 "Haswell" processors, each equipped with 12 cores operating at a frequency of 2.5 GHz. In figure 6 we give a brief overview of the numerical performance of the *FOM* simulation. We show in figure 6 a the number of Newton iterations in each time step. The number of Newton iterations is between three and nine. It is elevated to five during ventricular systole and rises to nine at end-systole, where the aortic valve closes. The number of linear solver iterations of each Newton iteration at a given time step is shown in figure 6 b. The number of linear iterations is between 20 and 60 and shows similar trends as the number of Newton iterations. This performance is reasonable and assures a good basis to which *ROM* simulations can be compared to. In the following, we compare exclusively simulation time and exclude time for creating the projection matrix  $\mathbf{V}$ . It is calculated once in a preliminary step using the same hardware and requires only about one minute.

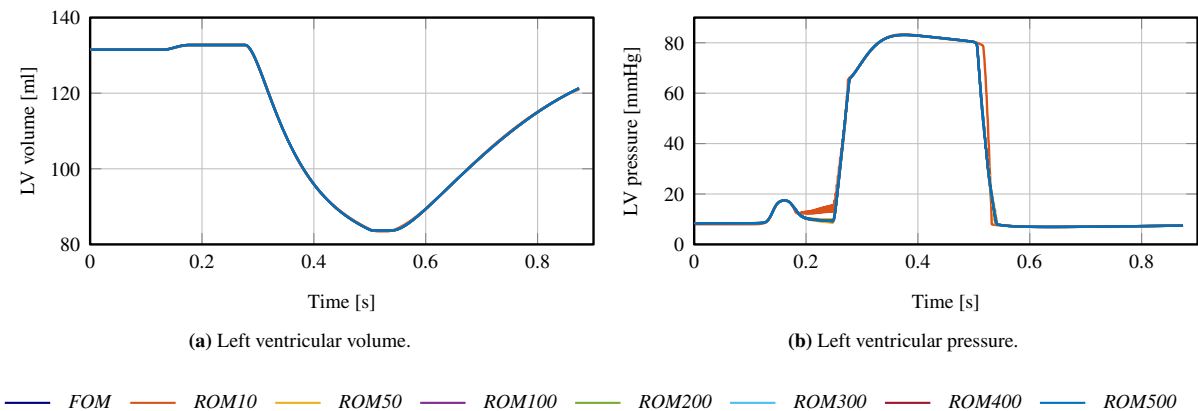


FIGURE 5 Scalar outputs of *FOM* and various *ROMs* over time.

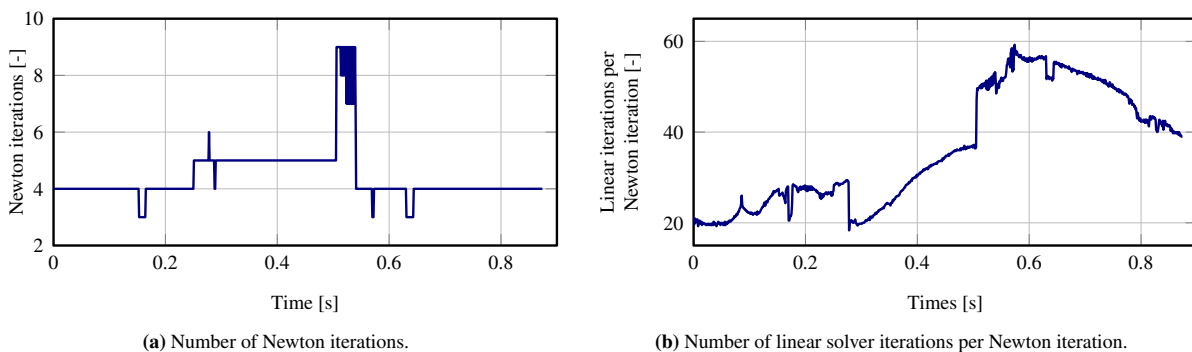


FIGURE 6 Solver performance of *FOM* in each time step.

The computation time of *ROM* simulations with various reduced orders  $q$  is compared to the total *FOM* simulation time in figure 7. Firstly, we show in figure 7 a the speedup factor  $\alpha$  of *ROM* over *FOM* simulations. The effect of *POD* is evident for *ROM* simulations between  $q = 500$  and  $q = 10$ , where we achieve a speedup of  $\alpha \approx 5$  and  $\alpha \approx 13$  over the *FOM* simulation, respectively. Note that while we achieve high speedups we did not lower hardware demands. The RAM consumption has actually increased slightly for *ROM* simulations, since we need to additionally store the projection matrix  $\mathbf{V}$ . This again motivates to pursue hyper-reduction in future studies.

We distinguish in figure 7 b between three components of total computation time. Component "Linear system" includes the time required for the multiplications of the projection matrix  $\mathbf{V}$  with the blocks of the Jacobian matrix in (12) as well as the time to solve the reduced linear system. This component strongly depends on the reduced order  $q$  as it scales with the complexity of the matrix-matrix multiplications, which is the main time contributor. The solution time of the reduced linear system itself is negligible. Component "Evaluate elements" contains time spent during element evaluation to assemble the block Jacobian matrix and the right-hand side. As expected, this component is independent of  $q$ , since we still build the full system before projecting it to the  $q$ -dimensional subspace. Component "Other" sums up all other time spent during the simulation, e.g. file input and output or general overhead, and is also independent of  $q$ .

In figure 7 c we show the relative distribution of simulation time for *FOM*, *ROM500*, and *ROM10*. For the 21 hours spent during a *FOM* simulation, 92% of simulation time are spent solving the linear system. This large proportion shows the potential for savings using *MOR* with *POD*. Reducing and solving the linear system in *ROM10* only makes up 4% of the simulation time. However, the new bottleneck is now the element evaluation at 63% of the simulation time. This, again, motivates the use of hyper-reduction methods, such as the discrete empirical interpolation method (DEIM)<sup>42</sup>, for *ROMs* with very few degrees of freedom.

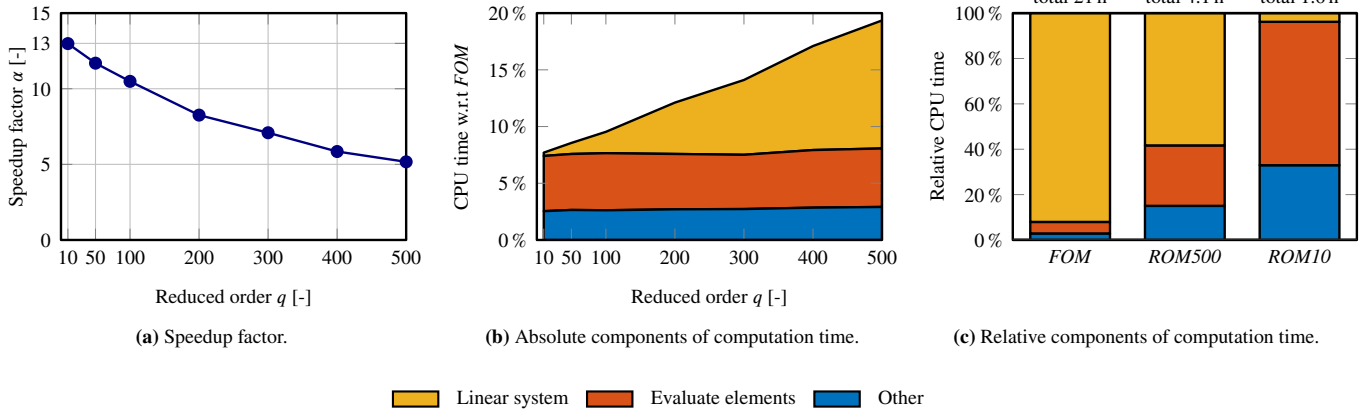


FIGURE 7 Simulation times of *FOM* and *ROM*.

## 4.2 | Parametric model order reduction

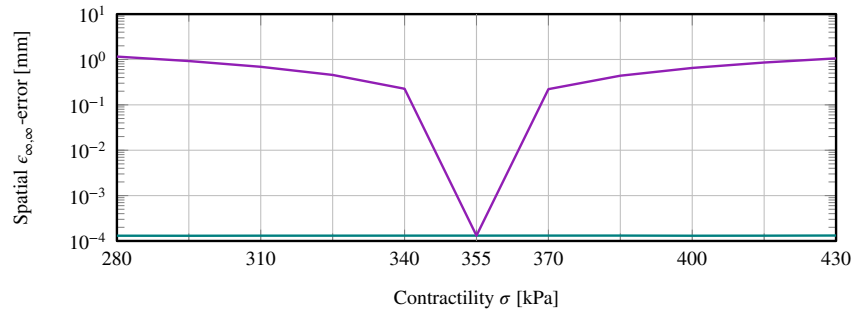
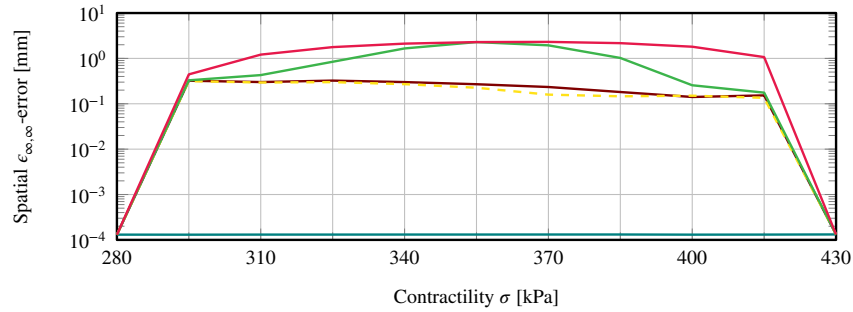
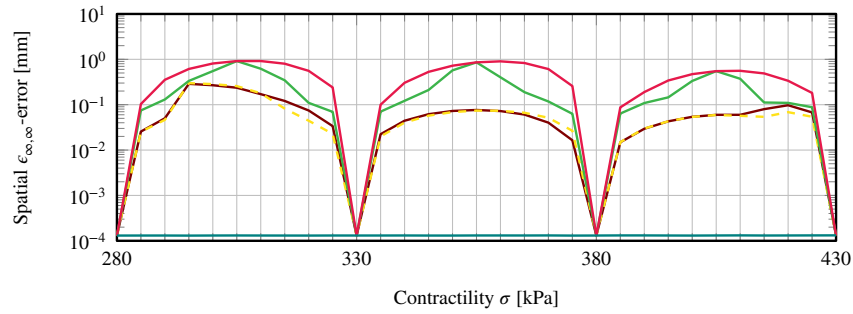
In this section we provide a quantitative comparison of several subspace interpolation methods introduced in section 3.3 for parametric model order reduction (*pMOR*) to demonstrate the ability to evaluate the *ROM* simulations at parameter sets without prior *FOM* knowledge. We vary the contractility  $\sigma$  in (3), controlling the upper limit of the myocardium's active stress in fiber direction. It is a key parameter of cardiac contraction and has a major influence on elastodynamics as well as on several scalar cardiac measures. It is commonly calibrated to match the end-systolic volume of the left ventricle as measured in cine MRI. In this work, we vary the contractility  $\sigma \in [280 \text{ kPa}, 430 \text{ kPa}]$ , as this range produces *FOM* simulation results that are in agreement with cine MRI. We use  $q = 300$  for all *ROM* simulations in this section, since it was shown in figure 4 b that no further improvements are made in approximation quality for  $q > 300$ . In section 4.2.1 we demonstrate the approximation quality with respect to the spatial displacement field. However, in many clinical applications a full solution of the displacements is not needed. We therefore show the approximation quality of *pMOR* with respect to scalar cardiac quantities of clinical significance in section 4.2.2.

### 4.2.1 | Approximation of displacements

In figure 8 we compare the spatial  $\epsilon_{\infty, \infty}$ -error for a varying contractility. We compare *pMOR* simulations using snapshots of *FOM* simulations from one, two, and four  $\sigma$ -sample points in figures 8 a, 8 b, and 8 c, respectively. As a reference, we additionally show the error obtained from direct *ROM* simulations, i.e. *ROM* simulations where we use a projection matrix  $\mathbf{V}(\sigma)$  from the corresponding *FOM* evaluation for each  $\sigma$ . This information is however not used in the *pMOR* solutions displayed here and would not be available in a typical *MOR* scenario, as it would render *MOR* useless. The direct *ROM* approximation error is mostly independent of the choice for parameter  $\sigma$ .

We show in figure 8 a the *MOR* approximation with varying  $\sigma$  and a constant projection matrix  $\mathbf{V}(\sigma_1)$  which was obtained from a single *FOM* simulation with sample point  $\sigma_1 = 355 \text{ kPa}$ . Technically, this would not be considered in *pMOR*, since the projection matrix is not adapted to the parameter set. It can be observed that *MOR* simulations with  $\sigma \neq \sigma_1$  provide reasonable results with a spatial error below 1 mm using  $\mathbf{V}(\sigma_1)$ . However, with an increasing range of the parameter interval, the additional effort of subspace interpolation becomes advantageous. The approximation error of *MOR* simulations using two and four sample points are displayed in figures 8 b and 8 c, respectively. Both studies show similar results. The error is highest between sample points and approaches the error of the direct *ROM* simulations close to the sample points. The *pMOR* approximation errors are reduced when using a finer resolution of sample points. The subspace interpolation with the largest spatial error is obtained by the Grassmannian manifold and concatenation of bases (CoB) methods, coinciding in the middle between two sample points. An error of one order of magnitude smaller is achieved by using the concatenation of snapshots (CoS) and the adjusted direct interpolation methods, staying well below a spatial  $\epsilon_{\infty, \infty}$ -error of 1 mm.

The reason for the good performance of the adjusted direct interpolation method is due to the *POD* of both snapshot matrices of the left and right sample point yielding modes that allow for a distinctive pairing according to the Modal Assurance Criterion.

(a) One sample point  $\sigma_1 = 355$  kPa, increment  $\Delta\sigma = 15$  kPa.(b) Two sample points  $\sigma_k = \{280, 430\}$  [kPa], increment  $\Delta\sigma = 15$  kPa.(c) Four sample points  $\sigma_k = \{280, 330, 380, 430\}$  [kPa], increment  $\Delta\sigma = 5$  kPa.

**FIGURE 8** Spatial  $\epsilon_{\infty,\infty}$ -error for direct *ROM300*, constant *ROM300*, and *pROM300* with different interpolation techniques for a varying number of sample points.

However, the same subspace can be spanned by two sets of orthogonal basis vectors which are not necessarily linearly dependent on each other. If the information of a mode related to the left sample point is scattered among various modes corresponding to the right sample point, the direct interpolation method will most probably yield considerably worse results.

The CoS method is in our case far superior to the CoB method. As outlined in section 3.3, the CoS method allows for a direct usage of the snapshots at the sample points, while the CoB method uses the projection matrices computed at the sample points. The projection matrices, as compared to the snapshots, contain no information about the relative importance of the modes. The snapshots thus contain more information about the dynamics of the system, enabling the CoS method to select a more suitably interpolated subspace than the CoB method. Note, however, that the CoS method can only be applied when using it in combination with an observation-based reduction technique like *POD*.

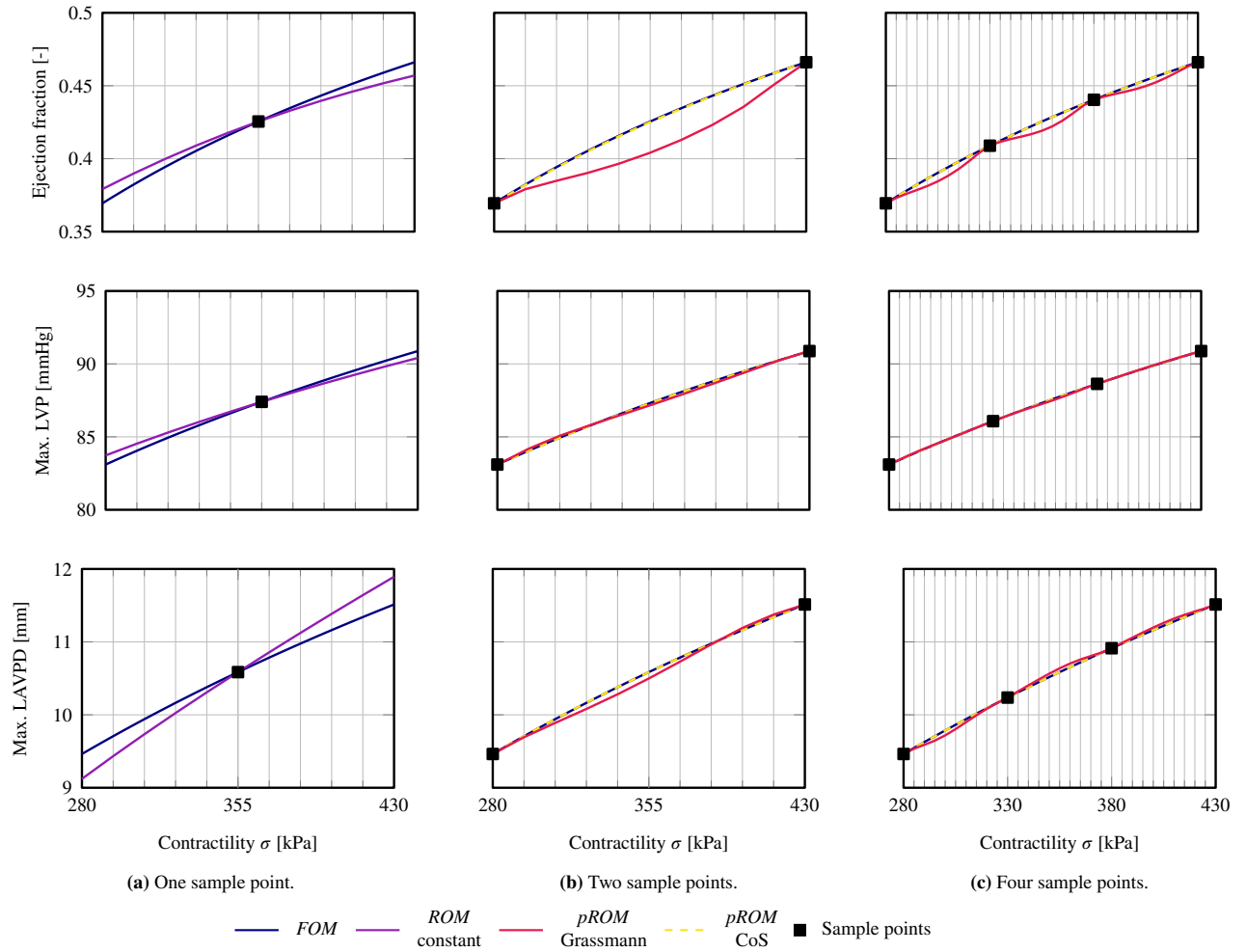


**FIGURE 9** Scalar cardiac quantities ejection fraction (top), maximal left ventricular pressure (middle), and maximal left atrioventricular plane displacement (bottom) for varying contractility  $\sigma$  in *FOM* and *ROM300*.

#### 4.2.2 | Approximation of scalar cardiac quantities

In figure 9 we show scalar output quantities of our cardiac model, evaluated for the same *MOR* simulations as in figure 8 using one, two, and four sample points in figures 9 a, 9 b, and 9 c, respectively. For each study we evaluate ejection fraction (EF), maximum left ventricular pressure (LVP), and maximum left atrioventricular plane displacement (LAVPD) and compare them to the *FOM* results. All three output quantities are important determinants of cardiac viability. They are also chosen because they allow us to study the approximation of different outputs of our coupled 3D-0D elasto-hemodynamical model with *pMOR*. EF, as defined in (22), is an integral value of the spatial displacement field, LVP is an output of the 0D windkessel model, and LAVPD is the average of a small subset of nodal directional displacements.

For one sample point we again compare the *FOM* solution in figure 9 a to the solution of a *ROM* using a constant projection matrix. The parameter dependence of the three cardiac quantities on  $\sigma$  is reproduced well by the constant *ROM* simulations. As expected, the deviations from the *FOM* solution are largest at evaluations furthest away from the sample point. However, the accuracy might still be sufficient for many applications. The cardiac quantities using two and four sample points are shown in figures 9 b and 9 c, respectively. For clarity, we show here only the results of the subspace interpolation methods which performed best and worst in figure 8, i.e. the CoS and Grassmann method, respectively. The outputs oscillate visibly between sample points when using the Grassmann interpolation method, improving as the resolution of sample points is refined. As in figure 8, the CoS method performs well, leading to a good approximation of the scalar cardiac quantities between sample points.

## 5 | APPLICATION TO INVERSE ANALYSIS

Models of cardiac elasto-hemodynamics commonly depend on a large set of parameters which need to be calibrated to patient-specific measurements using inverse analysis. This procedure is however computationally very expensive, as it requires many evaluations of the model (7), which will be denoted forward model in the following. We propose in this section a novel approach for gradient-based inverse analysis utilizing the parametric reduced order model (*pROM*) developed in section 4.2. We replace the *FOM* forward evaluations typically required for the finite differences to obtain the gradient by *pMOR* forward evaluations (12). We illustrate this method using a simple Levenberg-Marquardt (LM) algorithm<sup>43,44</sup> in section 5.1. The method however is applicable to any gradient-based optimization. In section 5.2 we demonstrate its performance on a typical inverse analysis scenario using the cardiac forward problem introduced in section 2.

### 5.1 | Parameter estimation based on reduced models

Given  $m$  normalized model outputs  $\mathbf{f}(\boldsymbol{\mu}) \in \mathbb{R}^m$  of a *FOM* depending on  $n_p$  normalized parameters  $\boldsymbol{\mu} \in \mathbb{R}^{n_p}$  and  $m \geq n_p$  normalized measurements  $\mathbf{y}$  we aim to minimize the squared sum  $S$  of residuals  $\mathbf{r}$

$$\hat{\boldsymbol{\mu}} = \underset{\boldsymbol{\mu}}{\operatorname{argmin}} S(\boldsymbol{\mu}), \quad \text{with } S(\boldsymbol{\mu}) = \frac{1}{2} \|\mathbf{r}(\boldsymbol{\mu})\|_2^2, \quad \mathbf{r}(\boldsymbol{\mu}) = \mathbf{y} - \text{FOM } \mathbf{f}(\boldsymbol{\mu}), \quad \mathbf{J}(\boldsymbol{\mu}) = \frac{\partial \mathbf{r}(\boldsymbol{\mu})}{\partial \boldsymbol{\mu}} \quad (23)$$

to obtain the optimal set of parameters  $\hat{\boldsymbol{\mu}}$ . The Jacobian of the residual vector with respect to the parameter vector is  $\mathbf{J} \in \mathbb{R}^{m \times n_p}$ . At the optimum  $\hat{\boldsymbol{\mu}}$ , the gradient  $\nabla S = \mathbf{J}^T \mathbf{r} = \mathbf{0}$  vanishes and the Hessian  $\nabla^2 S > \mathbf{0}$  is positive definite. Using the LM algorithm, we obtain the iterative procedure

$$\text{update } \boldsymbol{\mu}^{i+1} = \boldsymbol{\mu}^i + \Delta \boldsymbol{\mu}^{i+1}, \quad (24)$$

$$\text{with } \left[ \mathbf{J}^T \mathbf{J} + \lambda \operatorname{diag}(\mathbf{J}^T \mathbf{J}) \right]^i \cdot \Delta \boldsymbol{\mu}^{i+1} = - \left[ \mathbf{J}^T \mathbf{r} \right]^i, \quad \lambda^i = \lambda^{i-1} \cdot \frac{\|[\mathbf{J}^T \mathbf{r}]^i\|_2}{\|[\mathbf{J}^T \mathbf{r}]^{i-1}\|_2} \quad (25)$$

$$\text{until } \left\| [\mathbf{J}^T \mathbf{r}]^i \right\|_2 < \operatorname{tol}_{\text{grad}}^{\boldsymbol{\mu}} \quad \text{and} \quad \left\| \Delta \boldsymbol{\mu}^{i+1} \right\|_2 < \operatorname{tol}_{\text{inc}}^{\boldsymbol{\mu}}, \quad (26)$$

at iteration  $i+1$  with damping parameter  $\lambda$ . The LM algorithm approximates the Hessian as  $\nabla^2 S \approx \mathbf{J}^T \mathbf{J}$ . The damping parameter  $\lambda$  should tend to zero as the parameter set  $\boldsymbol{\mu}$  approaches the optimal solution  $\hat{\boldsymbol{\mu}}$ . For  $\lambda \rightarrow \infty$  we approach the steepest descent method, for  $\lambda = 0$  we obtain the Gauss-Newton method. In general, for a nonlinear model the analytical derivatives of the model evaluations  $\mathbf{f}$  with respect to the parameters  $\boldsymbol{\mu}$  required for the Jacobian matrix are not easily available. The  $n_p$  columns  $\mathbf{J}_p^i$  of the Jacobian matrix  $\mathbf{J}^i$  are thus typically approximated by finite differences

$$\mathbf{J}_p^i \approx \pm \frac{\text{pROM } \mathbf{f}(\boldsymbol{\mu}_{\Delta p}^i) - \text{pROM } \mathbf{f}(\boldsymbol{\mu}^i)}{\epsilon_p}, \quad \text{with } \boldsymbol{\mu}_{\Delta p}^i = \boldsymbol{\mu}^i \pm \epsilon_p \mathbf{e}_p, \quad \forall p \in [1, \dots, n_p] \quad (27)$$

The gradient evaluation vector  $\boldsymbol{\mu}_{\Delta p}^i$  is built from the  $p$ -th component  $\epsilon_p$  of a finite distance vector  $\boldsymbol{\epsilon} \in \mathbb{R}^p$  and the  $p$ -th unit vector  $\mathbf{e}_p \in \mathbb{R}^p$  in the direction of each parameter. The sign in (27) is chosen for each parameter  $p$  so that the evaluation with parameter set  $\boldsymbol{\mu}_{\Delta p}^i$  is within the range of all previously evaluated parameter sets.

Calculating the approximated Jacobian matrix requires  $n_p + 1$  evaluations of our forward model which is computationally expensive in case of a large number of parameters  $n_p$ . The *pROM* introduced in section 4.2 is very accurate for parameters in the proximity of the sampled parameter sets, as was shown in section 4.2.1 for the cardiac contractility parameter  $\sigma$ . More importantly, the *pMOR* evaluations shown in section 4.2.2 were not only able to accurately predict *FOM* scalar cardiac quantities but also their slope with respect to a changing contractility from only two *FOM* sample points. We therefore propose to use *pROM* evaluations of  $\mathbf{f}$  in (27) instead of *FOM* evaluations. The iterative procedure for the inverse analysis is sketched in algorithm 1. Note that while using this approach, we still find a local minimum of the objective function  $S$  in (23) with respect to the *FOM*.

Further note that with the strategy introduced in algorithm 1 the  $n_p + 1$  gradient evaluations using the *pROM* simulations can only be computed after a complete evaluation of the *FOM* simulation. Considering a scenario of infinite available computing resources, our strategy would actually slightly increase computation time over the standard approach of using the *FOM* for all evaluations, as all  $n_p + 1$  model evaluations can here be run in parallel. However, considering the more likely scenario where computing resources are just sufficient to calculate one or few *FOM* simulations at a time, the strategy outline in algorithm 1 leads to considerable time savings especially for a large number of parameters  $n_p$ .

Algorithm 1 can be combined with any subspace interpolation method in step 7. We use here the weighted concatenation of snapshots method (CoS) introduced in section A.2, as it performed best in the experiments in section 4.2 and is easily applicable

**Algorithm 1** Inverse analysis with  $pMOR$ -gradient

---

```

1: initialize  $\boldsymbol{\mu}^0, \lambda^0$ 
2:  $i = 0$ 
3: while convergence criterion from (26) not fulfilled do
4:   evaluate  $FOM \mathbf{f}(\boldsymbol{\mu}^i)$  and calculate residual  $\mathbf{r}^i$  from (23)
5:   store snapshots  $\mathbf{D}(\boldsymbol{\mu}^i)$ 
6:   for  $p = 0, \dots, n_p$  do
7:     build reduced basis  $\mathbf{V}(\boldsymbol{\mu}_{\Delta p}^i)$  from (28)
8:     evaluate  $pROM \mathbf{f}(\boldsymbol{\mu}_{\Delta p}^i)$ 
9:   end for
10:  calculate Jacobian  $\mathbf{J}^i$  from (27)
11:  update parameter vector  $\boldsymbol{\mu}^{i+1}$  from (25)
12:   $i \leftarrow i + 1$ 
13: end while
14: return  $\hat{\boldsymbol{\mu}} = \boldsymbol{\mu}^i$ 

```

---

to high dimensions of  $n_p$ . For the weights of the snapshot matrix for gradient evaluation  $p$ , we use a simple inverse distance weighting between two evaluation points

$$\begin{aligned} \tilde{\mathbf{D}}(\boldsymbol{\mu}_{\Delta p}^i) &= [w_1 \mathbf{D}(\boldsymbol{\mu}^i), w_2 \mathbf{D}(\boldsymbol{\mu}^k)], \quad w_1 = \frac{1/d_1}{1/d_1 + 1/d_2}, \quad w_2 = 1 - w_1, \\ d_1 &= \|\boldsymbol{\mu}_{\Delta p}^i - \boldsymbol{\mu}^i\|_2, \quad d_2 = \|\boldsymbol{\mu}_{\Delta p}^i - \boldsymbol{\mu}^k\|_2, \quad k = \underset{j \in \{0, \dots, i-1\}}{\operatorname{argmin}} \|\boldsymbol{\mu}_{\Delta p}^i - \boldsymbol{\mu}^j\|_2, \end{aligned} \quad (28)$$

with normalized distances  $d_1, d_2$  and weights  $w_1, w_2$  for the current evaluation  $i$  and the next closest evaluation  $k$ , respectively. Since at the beginning of the iteration  $\epsilon_p \ll |\boldsymbol{\mu}_p^i - \boldsymbol{\mu}_p^k|$ , the weight  $w_1$  of the current snapshot matrix  $\mathbf{D}(\boldsymbol{\mu}^i)$  is always close to one, whereas the weight  $w_2$  is close to zero. This can be interpreted that we "enrich" the snapshots of the current iteration with snapshots from a previous iteration to represent parametric dependence. As the optimization converges and the changes in parameters are close to the step size of the finite differences, the weights  $w_1$  and  $w_2$  equalize. For the first iteration of the optimization we rely on standard  $MOR$  evaluations using the constant projection matrix from the first  $FOM$  evaluation.

In the following, we give an equation for the speedup of gradient-based inverse analysis achieved by using  $pROM$  evaluations for the calculation of the Jacobian with respect to CPU time. Note that actual computation time depends on parallelization of model evaluations. We compare CPU time required to achieve convergence after  $n_i$  iterations for a model with gradients calculated from  $pROM$  and  $FOM$  forward model evaluations, denoted by superscript  $pROM$  and  $FOM$ , respectively. We do not include the time spent during subspace generation, as it is negligibly small compared to  $pROM$  and  $FOM$  evaluation time. The total CPU times  $T$  are

$$T^{FOM} = n_i^{FOM} (n_p + 1) t^{FOM}, \quad (29)$$

$$T^{pROM} = n_i^{pROM} [t^{FOM} + (n_p + 1) t^{pROM}], \quad (30)$$

where  $t$  is the time required for a single forward evaluation. It can be observed from (30) that the number of parameters only scales the  $pROM$  evaluation time but not the  $FOM$  evaluation time. Using the speedup  $\alpha$  of a single  $pROM$  evaluation over a  $FOM$  evaluation, we obtain the total speedup  $\beta$  for the inverse problem with respect to CPU time as

$$\beta = \frac{T^{FOM}}{T^{pROM}} = \underbrace{\frac{n_i^{FOM}}{n_i^{pROM}}}_{\approx 1} \cdot \underbrace{\frac{1}{\frac{1}{\alpha} + \frac{1}{1+n_p}}}_{\rightarrow \alpha \text{ for } n_p \rightarrow \infty}, \quad \text{with } \alpha = \frac{t^{FOM}}{t^{pROM}}. \quad (31)$$

As will be shown in section 5.2, the first factor is close to one as the number of iterations is comparable for both approaches when using a reasonably large number of reduced modes  $q$ . The second factor approaches  $\alpha$  in the case of many parameters. Note that in practice there is a trade-off between the two factors. Choosing a very low-dimensional reduced model with few degrees of freedom  $q$  results in a high single call speedup  $\alpha$  but may increase the number of iterations for the inverse analysis,



	$\sigma$ [kPa]	$\alpha_{\max}$ $\left[\frac{1}{s}\right]$	$\alpha_{\min}$ $\left[\frac{1}{s}\right]$	$t_{\text{sys}}$ [s]	$t_{\text{dias}}$ [s]
Initial	200	15	-15	0.35	0.60
Ground truth	280	10	-30	0.25	0.50

**TABLE 1** Initial values and ground truth of estimated parameters during inverse analysis ( $n_p = 5$ ).

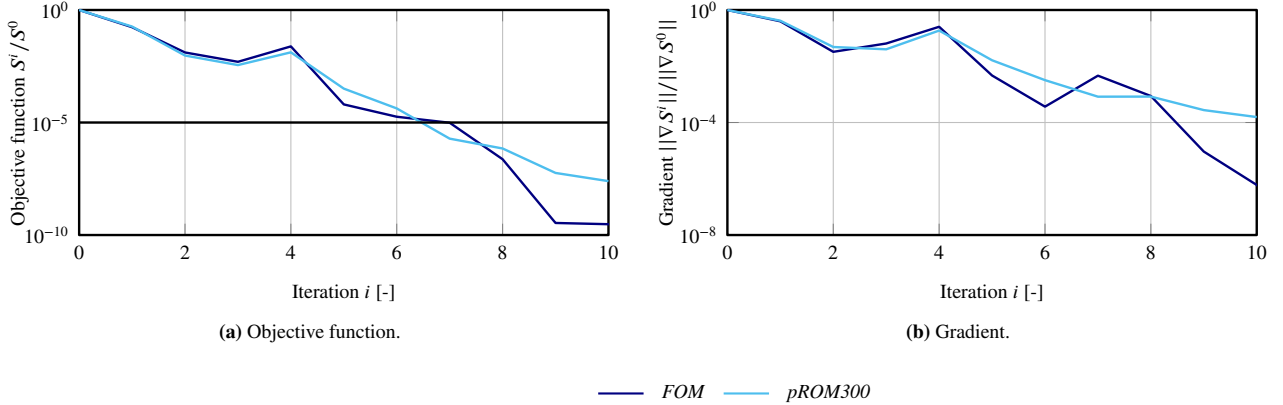


**FIGURE 10** Convergence behavior during gradient-based inverse analysis with finite differences for gradient calculation. Shown are objective function and gradient for each iteration, comparing the use of *FOM* and *pROM* for gradient calculation.

as the tangents are now approximated worse than with a higher  $q$ . Further note that, after their respective number of iterations, both approximations achieve the same convergence criterion, which is always evaluated using the *FOM*.

Other variants of algorithm 1 are feasible, e.g. replacing all *FOM* evaluations by *pROM* approximations as the inverse analysis algorithm converges closer to the optimum. Such algorithms however require more advanced strategies to switch between both model evaluations. The algorithm presented here demonstrates the most simple and straightforward approach of including a *pROM* within a finite difference gradient-based inverse analysis.

## 5.2 | Numerical results

We demonstrate the ability of the inverse analysis method proposed in section 5.1 to accurately and efficiently estimate parameters for a real-world cardiac estimation problem. We consider the case of a cardiac simulation which we want to calibrate to a given volume curve, i.e. measurements of left ventricular volume over time during one cardiac cycle. We have no prior solutions of our *FOM* and thus need to build our projection matrices from scratch starting at the first iteration of algorithm 1.

We choose the solution displayed in figure 5 a of a forward *FOM* simulation as our ground truth. As parameters we choose contractility  $\sigma$  from (3) and myofiber activation rate  $\alpha_{\max}$ , myofiber deactivation rate  $\alpha_{\min}$ , onset of ventricular systole  $t_{\text{sys}}$ , and onset ventricular diastole  $t_{\text{dias}}$  from (4). We thus estimate all parameters necessary to determine the shape of the input function of our model, i.e. the active stress over time  $\tau(t)$ . The parameters  $\sigma$ ,  $\alpha_{\max}$ , and  $\alpha_{\min}$  control cardiac output. However, due to their large variation they are commonly calibrated to a given patient<sup>25</sup>. These parameters are interconnected with the timing parameters  $t_{\text{sys}}$  and  $t_{\text{dias}}$ . The non-normalized parameters at the start of the inverse analysis and of the ground truth are listed in table 1. We initialize the damping parameter  $\lambda^0 = 0.1$ . We further choose the number of reduced modes  $q = 300$  as it offers a good trade-off between accuracy and speedup.

In figure 10 we display the performance of the *pROM* inverse analysis using algorithm 1 compared to the standard approach where the gradients are evaluated using the *FOM* only. Figure 10 a shows the decay of the objective function  $S$  from (23). We define a convergence criterion  $S^i/S^0 < 10^{-5}$ , which is achieved at  $n_i^{\text{FOM}} = n_i^{\text{pROM}} = 7$ . In figure 10 b we compare the development of the gradient of the objective function with respect to the parameters. As we consider a synthetic case in the absence of noise, both objective function and gradient should approach zero as  $i \rightarrow \infty$ . As both measures are non-monotonically

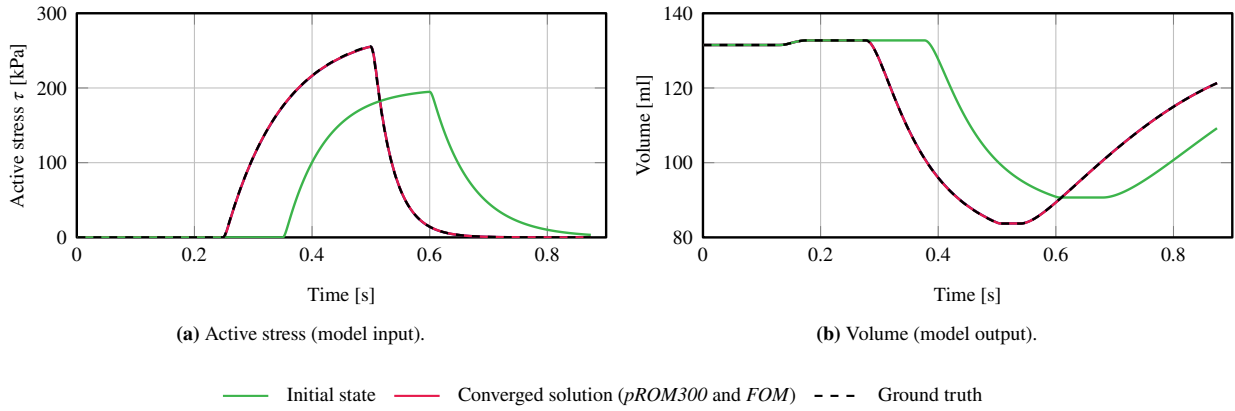


**FIGURE 11** Initial state, converged solution, and ground truth of inverse analysis for model input (active stress) and model output (volume) over time.

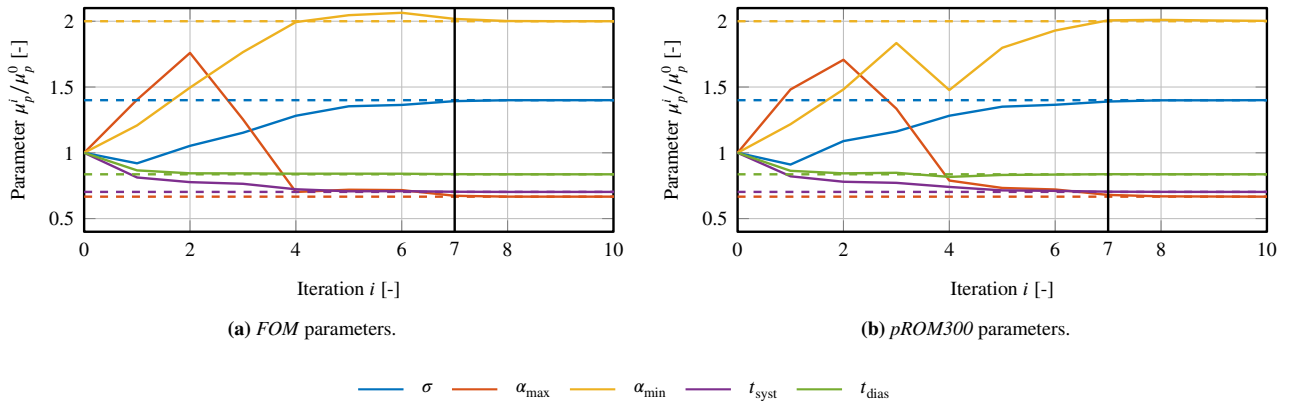


**FIGURE 12** Convergence of parameters in inverse analysis. Dotted lines indicate ground truth of parameter.

decreasing, this indicates a non-smooth optimization problem. However, the  $pROM300$ -gradient optimization is in excellent agreement with the  $FOM$ -gradient optimization.

The start, ground truth, and the converged solutions of both methods after seven iterations are shown in figure 11. Here, the activation function, i.e. the input of our model, and the volume, i.e. the output of our model, are shown in figures 11 a and 11 b, respectively. It can be observed that both optimization methods match well with ground truth data for the given convergence criterion. The convergence of the five parameters relative to their initial values is shown in figure 12 for both methods. Additionally, the iteration where the convergence criterion is achieved is indicated. Both methods show a similar trend towards the optimal parameters. With a single evaluation speedup of  $\alpha \approx 7.1$ , we obtain an overall speedup in CPU time of the  $pROM300$  method over the  $FOM$  method of  $\beta \approx 3.3$ , since  $n_i^{FOM}/n_i^{ROM} = 1$  and  $n_p = 5$  in our case. evaluate the gradients reduces CPU time by 69% while achieving the same accuracy.

## 6 | CONCLUSIONS

In this work we proposed a new projection-based reduced order model for coupled structure-windkessel cardiac models, where we solely reduced the large structural dimension. Specifically, we used a nonlinear large deformation cardiac finite element model with pericardial boundary conditions. For subspace generation, we employed proper orthogonal decomposition ( $POD$ ) applied to displacement snapshots of the full order model ( $FOM$ ). We demonstrated the accuracy and speedup of the reduced order model ( $ROM$ ) for a range of reduced dimensions  $q \in \{10, \dots, 500\}$ . In that range, the approximation error was found to be

between  $2 \cdot 10^{-1}$  mm and  $1 \cdot 10^{-4}$  mm, which is well below the resolution of state of the art cardiac imaging employed in current clinical practice. For these simulations, we achieved speedups between 13 and 5 over our *FOM*. For highly reduced models, it was shown that the new bottleneck in simulation time is element evaluation. This motivates the inclusion of hyper-reduction methods, such as the discrete empirical interpolation method (DEIM)<sup>42</sup> or the energy conserving mesh sampling and weighting method (ECSW)<sup>21</sup>, in future research. As the kinematics of a patient-specific heart can already be observed in motion MRI, it might be conceivable to incorporate this displacement information in the reduced space.

There exist many potential applications of *MOR* in cardiac many-query settings. One example is the task of obtaining a physiological periodic state, i.e. where left and right ventricular output per cardiac cycle match. In these scenarios, a cardiac simulation with constant parameters is run for multiple cycles, until the change from one cycle to the next is below a given tolerance. In<sup>10</sup> it was reported that in some cases more than ten cycles were necessary until converge to a periodic state. After simulating one *FOM* cycle and calculating the projection matrix, all preceding cycles could be run using a *ROM* since the shape of the cardiac contraction will be similar to the first cycle. In this use case, *MOR* can lead to drastic time savings, especially as the individual cardiac cycles cannot be run in parallel.

We further compared four different methods of parametric model order reduction (*pMOR*) to allow *ROM* evaluations at parameter sets without prior *FOM* knowledge. The *pMOR* methods were evaluated by varying cardiac contractility, an important determinant of cardiac performance. The weighted concatenation of snapshots method was found to approximate the displacements of the *FOM* best for this example. Additionally, we showed that the clinically important scalar cardiac quantities ejection fraction, maximum left ventricular pressure, and left atrioventricular plane displacement are also well approximated using *pMOR*. Next to model calibration and design exploration, a possible application of cardiac *pMOR* could be multifidelity uncertainty quantification<sup>9</sup>.

Finally, we introduced a novel method to include *pMOR* into a finite difference gradient-based inverse analysis. Using the Levenberg-Marquardt algorithm as an example, we proposed to use the *FOM* for all objective function evaluations and *pMOR* for all gradient evaluations, based on snapshots from the current and previous iterations. Using synthetic data in a real-world inverse analysis scenario, we demonstrated that *pMOR*-gradient-based optimization shows the same convergence properties as *FOM*-gradient-based optimization while achieving considerable CPU time savings. This method can be incorporated easily into existing optimization frameworks and could even be combined with commercial solvers for the structural problem. Using the inverse analysis approach proposed here has the advantage that we still calculate a full displacement field in each evaluation of the forward model. We can thus evaluate any spatial quantity, which is not possible when using 2D, 1D, or 0D surrogate models for the 3D structural model. In future research, this will allow us to compute a spatial approximation error with respect to cine or tagged MRI to estimate patient-specific parameters from clinical observations. To further improve *pMOR*-based gradient evaluation, we will include *pMOR*-gradients in a tailored optimization algorithm that benefits from multiple cheap gradient and second-derivative evaluations to speed up convergence.



## APPENDIX

### A SUBSPACE INTERPOLATION METHODS

In this appendix, we give a thorough mathematical description of the subspace interpolation methods utilized in this work. For a comprehensive review on these and other methods of parametric model order reduction, the reader is referred to<sup>19</sup>.

#### A.1 Weighted concatenation of bases

A common and straightforward approach to obtain a global basis matrix  $\mathbf{V}$  from the precomputed local bases  $\mathbf{V}(\boldsymbol{\mu}_1), \dots, \mathbf{V}(\boldsymbol{\mu}_K)$  is given by the method “concatenation of bases”. With this technique, the local bases are at first simply concatenated side-by-side, followed by a SVD of the resulting matrix to compute the global basis  $\mathbf{V}$ . This technique can be extended by introducing the weighting functions  $w_k(\boldsymbol{\mu}^*)$  in the concatenation of bases, in order to compute a *parameter-dependent* interpolated basis  $\mathbf{V}(\boldsymbol{\mu}^*)$  which takes the distance of the new query point  $\boldsymbol{\mu}^*$  with respect to the sample points  $\boldsymbol{\mu}_1, \dots, \boldsymbol{\mu}_K$  into account. To this end, the matrices  $\mathbf{V}(\boldsymbol{\mu}_1), \dots, \mathbf{V}(\boldsymbol{\mu}_K)$  are first weighted with weights  $w_k(\boldsymbol{\mu}^*)$  and concatenated afterwards. Then, the SVD of the

concatenated matrix  $\tilde{\mathbf{V}}(\boldsymbol{\mu}^*)$

$$\tilde{\mathbf{V}}(\boldsymbol{\mu}^*) = [w_1(\boldsymbol{\mu}^*) \mathbf{V}(\boldsymbol{\mu}_1), \dots, w_K(\boldsymbol{\mu}^*) \mathbf{V}(\boldsymbol{\mu}_K)] = \tilde{\mathbf{U}}(\boldsymbol{\mu}^*) \tilde{\boldsymbol{\Sigma}}(\boldsymbol{\mu}^*) \tilde{\mathbf{T}}(\boldsymbol{\mu}^*)^T \in \mathbb{R}^{n \times K \cdot q} \quad (\text{A1})$$

is performed. The interpolated basis  $\mathbf{V}(\boldsymbol{\mu}^*)$  is finally constructed by considering the first  $q$  left singular vectors  $\{\tilde{\mathbf{u}}_i(\boldsymbol{\mu}^*)\}_{i=1}^q$  that best represent the weighted and concatenated matrix  $\tilde{\mathbf{V}}(\boldsymbol{\mu}^*)$ :

$$\mathbf{V}(\boldsymbol{\mu}^*) = [\tilde{\mathbf{u}}_1(\boldsymbol{\mu}^*), \dots, \tilde{\mathbf{u}}_q(\boldsymbol{\mu}^*)] \in \mathbb{R}^{n \times q}. \quad (\text{A2})$$

Please note that the described weighting procedure is purely optional. The advantage of the weighted approach is that subspaces near the interpolation point  $\boldsymbol{\mu}^*$  are favored and stronger considered than subspaces describing the dynamics for far-distant sample points. However, this extended technique requires more computational effort than the classical concatenation approach, since a SVD has to be performed for every new  $\boldsymbol{\mu}^*$  to compute the parameter-dependent interpolated basis  $\mathbf{V}(\boldsymbol{\mu}^*)$ .

## A.2 Weighted concatenation of snapshots

The concatenation of bases approach explained in the previous section provides a basis  $\mathbf{V}(\boldsymbol{\mu}^*)$  comprising the most important directions among the (weighted) basis vectors from all local bases. Note, however, that the bases  $\mathbf{V}(\boldsymbol{\mu}_k) = \mathbf{U}(\boldsymbol{\mu}_k)(: , 1 : q)$  for  $k = 1, \dots, K$  are calculated in our case by means of the SVD-based technique of *POD* and they, therefore, essentially approximate the snapshot matrices  $\mathbf{D}(\boldsymbol{\mu}_k)$

$$\mathbf{D}(\boldsymbol{\mu}_k) = \mathbf{U}(\boldsymbol{\mu}_k) \boldsymbol{\Sigma}(\boldsymbol{\mu}_k) \mathbf{T}(\boldsymbol{\mu}_k)^T. \quad (\text{A3})$$

Since we are actually most interested in finding a basis that optimally approximates the system dynamics over a range of parameters, in our concrete *POD*-case it seems very reasonable to construct the interpolated basis  $\mathbf{V}(\boldsymbol{\mu}^*)$  from a (weighted) concatenation of snapshots rather than from a (weighted) concatenation of bases. With the former technique, the matrix  $\mathbf{V}(\boldsymbol{\mu}^*)$  is therefore constructed by considering the first  $q$  left singular vectors of the (weighted and) concatenated snapshot matrix  $\tilde{\mathbf{D}}(\boldsymbol{\mu}^*)$ :

$$\tilde{\mathbf{D}}(\boldsymbol{\mu}^*) = [w_1(\boldsymbol{\mu}^*) \mathbf{D}(\boldsymbol{\mu}_1), \dots, w_K(\boldsymbol{\mu}^*) \mathbf{D}(\boldsymbol{\mu}_K)] = \tilde{\mathbf{U}}_{\tilde{\mathbf{D}}}(\boldsymbol{\mu}^*) \tilde{\boldsymbol{\Sigma}}_{\tilde{\mathbf{D}}}(\boldsymbol{\mu}^*) \tilde{\mathbf{T}}_{\tilde{\mathbf{D}}}(\boldsymbol{\mu}^*)^T \in \mathbb{R}^{n \times K \cdot n_s}. \quad (\text{A4})$$

### Remark: Connection between the concatenation methods

It can be shown that the just described (weighted) concatenation of snapshots approach corresponds to a *modified* (weighted) concatenation of bases, where each vector  $\mathbf{v}_i(\boldsymbol{\mu}_k)$  is (further) weighted with the corresponding singular value  $\sigma_i(\boldsymbol{\mu}_k)$  for all non-zero singular values. Thus, the first  $q$  left singular vectors of the – towards equation (A1) – modified matrix  $\tilde{\mathbf{V}}(\boldsymbol{\mu}^*)$

$$\tilde{\mathbf{V}}(\boldsymbol{\mu}^*) = [w_1(\boldsymbol{\mu}^*) \mathbf{V}(\boldsymbol{\mu}_1) \boldsymbol{\Sigma}_q(\boldsymbol{\mu}_1), \dots, w_K(\boldsymbol{\mu}^*) \mathbf{V}(\boldsymbol{\mu}_K) \boldsymbol{\Sigma}_q(\boldsymbol{\mu}_K)] = \tilde{\mathbf{U}}(\boldsymbol{\mu}^*) \tilde{\boldsymbol{\Sigma}}(\boldsymbol{\mu}^*) \tilde{\mathbf{T}}(\boldsymbol{\mu}^*)^T, \quad (\text{A5})$$

where  $\boldsymbol{\Sigma}_q(\boldsymbol{\mu}_k) = \boldsymbol{\Sigma}(\boldsymbol{\mu}_k)(1 : q, 1 : q) \in \mathbb{R}^{q \times q}$ , span the same interpolated subspace  $\mathcal{V}(\boldsymbol{\mu}^*)$  than the  $q$  leading vectors in  $\tilde{\mathbf{U}}_{\tilde{\mathbf{D}}}(\boldsymbol{\mu}^*)$ .

## A.3 Adjusted direct basis interpolation

It is well-known that a straightforward interpolation of the basis vectors comprised in the local projection matrices  $\mathbf{V}(\boldsymbol{\mu}_1), \dots, \mathbf{V}(\boldsymbol{\mu}_K)$  does generally not yield a meaningful basis. This is due to the fact that the basis vectors  $\{\mathbf{v}_i(\boldsymbol{\mu}_k)\}_{i=1}^q$  for different sample points span diverse subspaces, thus having a distinct physical interpretation and possibly pointing even in opposite directions in space. Therefore, the basis vectors should be first arranged to point in similar directions, thus spanning similar subspaces, before their entries are interpolated. This adjustment is performed using the Modal Assurance Criterion (MAC)<sup>45,46</sup>

$$\text{MAC}(\mathbf{v}_i, \mathbf{v}_j) = \frac{|\mathbf{v}_i^T \cdot \mathbf{v}_j|^2}{\|\mathbf{v}_i\|_2^2 \cdot \|\mathbf{v}_j\|_2^2} \in [0, 1], \quad (\text{A6})$$

which provides a measure for the similarity or linear dependence between the vectors  $\mathbf{v}_i$  and  $\mathbf{v}_j$ . The maximal value of the MAC is 1, which corresponds to linear dependent vectors, whereas orthogonal vectors take the minimal value 0. Hence, the idea is to only interpolate vectors which are strongly correlated to each other and maximize the MAC. To do so, we first have to select a reference subspace with respect to which the adjustment of the bases should be performed. The reference subspace, spanned by the columns of  $\mathbf{R}_V \in \mathbb{R}^{n \times q}$ , should ideally comprise the most important dynamics among all parameter sample points and be representative for all local bases. The simplest way to select  $\mathbf{R}_V$  is to take one particularly important local basis  $\mathbf{R}_V = \mathbf{V}_{k_0}$  with  $k_0 \in \{1, \dots, K\}$ . Another possibility is to construct the reference subspace similarly as described in section A.1, i.e. using

the (weighted) concatenation of bases approach, yielding  $\mathbf{R}_V = \tilde{\mathbf{U}}(:, 1 : q)$  or  $\mathbf{R}_V(\boldsymbol{\mu}^*) = \tilde{\mathbf{U}}(\boldsymbol{\mu}^*)(:, 1 : q)$ . Once the reference subspace has been selected, the vectors  $\mathbf{v}_{i^*(j,k)}(\boldsymbol{\mu}_k)$  that fulfill

$$i^*(j, k) = \underset{i}{\operatorname{argmax}} \operatorname{MAC}(\mathbf{v}_i(\boldsymbol{\mu}_k), \mathbf{R}_V(:, j)) \quad \text{for } j = 1, \dots, q \text{ and } k = 1, \dots, K \quad (\text{A7})$$

are taken to be interpolated. Furthermore, the orientation of the vectors  $\mathbf{v}_{i^*(j,k)}(\boldsymbol{\mu}_k)$  and  $\mathbf{R}_V(:, j)$  is equalized by adapting the sign, in order to avoid that an interpolation between vectors pointing in (almost) opposite directions results in a mutual cancellation. Finally, the interpolation of the vectors is given by

$$\bar{\mathbf{v}}_j(\boldsymbol{\mu}^*) = \sum_{k=1}^K w_k(\boldsymbol{\mu}^*) \cdot [\pm \mathbf{v}_{i^*(j,k)}(\boldsymbol{\mu}_k)] \quad \text{with} \quad \sum_{k=1}^K w_k(\boldsymbol{\mu}^*) = 1. \quad (\text{A8})$$

The interpolation of orthonormal vectors does not necessarily yield a set of orthonormal vectors. Therefore, the interpolated vectors  $\{\bar{\mathbf{v}}_j(\boldsymbol{\mu}^*)\}_{j=1}^q$  are subsequently orthonormalized by employing the SVD of  $\bar{\mathbf{V}}(\boldsymbol{\mu}^*)$

$$\bar{\mathbf{V}}(\boldsymbol{\mu}^*) = [\bar{\mathbf{v}}_1(\boldsymbol{\mu}^*), \dots, \bar{\mathbf{v}}_q(\boldsymbol{\mu}^*)] = \bar{\mathbf{U}}(\boldsymbol{\mu}^*) \bar{\boldsymbol{\Sigma}}(\boldsymbol{\mu}^*) \bar{\mathbf{T}}(\boldsymbol{\mu}^*)^T \quad (\text{A9})$$

and considering the first  $q$  left singular vectors  $\{\bar{\mathbf{u}}_j(\boldsymbol{\mu}^*)\}_{j=1}^q$  for the interpolated basis  $\mathbf{V}(\boldsymbol{\mu}^*) \in \mathbb{R}^{n \times q}$ .

### Special case of two precomputed bases and one parameter

In order to make the afore explained method more clear, we now briefly present the special case of two precomputed bases ( $K = 2$ ) and one single parameter ( $n_p = 1$ ). Let us assume that bases  $\mathbf{V}(\mu_1)$  and  $\mathbf{V}(\mu_2)$  have been computed at the parameter sample points  $\mu_1$  and  $\mu_2$ , and that the new parameter value  $\mu^*$  lies between these two samples. Suppose that we choose the reference basis e.g. as  $\mathbf{R}_V = \mathbf{V}(\mu_2)$ . Then, the vectors  $\mathbf{v}_{i^*(j)}(\mu_1)$  that fulfill

$$i^*(j) = \underset{i}{\operatorname{argmax}} \operatorname{MAC}(\mathbf{v}_i(\mu_1), \mathbf{v}_j(\mu_2)) \quad \text{for } j = 1, \dots, q \quad (\text{A10})$$

are selected to be combined with the vectors  $\mathbf{v}_j(\mu_2)$ . The interpolation reads

$$\bar{\mathbf{v}}_j(\boldsymbol{\mu}^*) = w(\boldsymbol{\mu}^*) \cdot [\pm \mathbf{v}_{i^*(j)}(\mu_1)] + (1 - w(\boldsymbol{\mu}^*)) \cdot \mathbf{v}_j(\mu_2) \quad (\text{A11})$$

with the weight

$$w(\boldsymbol{\mu}^*) = \frac{\mu^* - \mu_2}{\mu_1 - \mu_2} \in [0, 1] \quad \text{for } \mu^* \in [\mu_1, \mu_2], \quad (\text{A12})$$

providing that a linear interpolation is employed.

## A.4 Basis interpolation on a Grassmannian manifold

As discussed before, a direct interpolation of the local bases is not meaningful, since they span different subspaces. In addition to the afore explained adjustment of the bases before interpolation, one may also interpolate the underlying subspaces on a tangent space of a manifold. The method proposed by Amsallem and Farhat<sup>20</sup> constructs a basis matrix  $\mathbf{V}(\boldsymbol{\mu}^*)$  for a new parameter point  $\boldsymbol{\mu}^*$  by interpolating the subspaces corresponding to the bases  $\{\mathbf{V}(\boldsymbol{\mu}_k)\}_{k=1}^K$  on the tangent space to the Grassmannian manifold  $\mathcal{G}_q(\mathbb{R}^n)$ .

The first step of the approach consists in choosing a local basis matrix  $\mathbf{V}_{k_0}$  for the reference point  $\mathcal{V}_{k_0} \in \mathcal{G}_q(\mathbb{R}^n)$ , at which the tangent space  $\mathcal{T}_{\mathcal{V}_{k_0}}$  to the manifold  $\mathcal{G}_q(\mathbb{R}^n)$  is constructed. Afterwards, all subspaces  $\mathcal{V}(\boldsymbol{\mu}_k)$  spanned by the local bases  $\mathbf{V}(\boldsymbol{\mu}_k)$  are mapped onto this tangent space by the so-called logarithmic mapping:  $\operatorname{span}(\boldsymbol{\Gamma}_k) = \operatorname{Log}_{\mathcal{V}_{k_0}}(\mathcal{V}_k) \in \mathcal{T}_{\mathcal{V}_{k_0}}$ . This is done basically by computing  $K$  thin SVDs

$$(\mathbf{I} - \mathbf{V}_{k_0} \mathbf{V}_{k_0}^T) \mathbf{V}(\boldsymbol{\mu}_k) (\mathbf{V}_{k_0}^T \mathbf{V}(\boldsymbol{\mu}_k))^{-1} = \mathbf{U}(\boldsymbol{\mu}_k) \boldsymbol{\Sigma}(\boldsymbol{\mu}_k) \mathbf{T}(\boldsymbol{\mu}_k)^T \quad \text{for } k = 1, \dots, K \quad (\text{A13})$$

and then calculating

$$\boldsymbol{\Gamma}(\boldsymbol{\mu}_k) = \mathbf{U}(\boldsymbol{\mu}_k) \arctan(\boldsymbol{\Sigma}(\boldsymbol{\mu}_k)) \mathbf{T}(\boldsymbol{\mu}_k)^T. \quad (\text{A14})$$

In order to compute the orthonormal basis  $\mathbf{V}(\boldsymbol{\mu}^*)$  for a new parameter point  $\boldsymbol{\mu}^*$ , the matrices  $\{\boldsymbol{\Gamma}(\boldsymbol{\mu}_k)\}_{k=1}^K$  are first interpolated using the weights  $w_k(\boldsymbol{\mu}^*)$  to obtain

$$\boldsymbol{\Gamma}^* = \boldsymbol{\Gamma}(\boldsymbol{\mu}^*) = \sum_{k=1}^K w_k(\boldsymbol{\mu}^*) \boldsymbol{\Gamma}(\boldsymbol{\mu}_k). \quad (\text{A15})$$

The interpolated subspace  $\text{span}(\boldsymbol{\Gamma}^*) \in \mathcal{T}_{\mathcal{V}_{k_0}}$  is then mapped back to the original manifold  $\mathcal{G}_q(\mathbb{R}^n)$  by the so-called exponential mapping:  $\mathcal{V}(\boldsymbol{\mu}^*) = \text{Exp}_{\mathcal{V}_{k_0}}(\text{span}(\boldsymbol{\Gamma}^*)) \in \mathcal{G}_q(\mathbb{R}^n)$ . The back-mapping step is numerically achieved by computing a thin SVD

$$\boldsymbol{\Gamma}(\boldsymbol{\mu}^*) = \mathbf{U}(\boldsymbol{\mu}^*) \boldsymbol{\Sigma}(\boldsymbol{\mu}^*) \mathbf{T}(\boldsymbol{\mu}^*)^T, \quad (\text{A16})$$

followed by

$$\mathbf{V}(\boldsymbol{\mu}^*) = \mathbf{V}_{k_0} \mathbf{T}(\boldsymbol{\mu}^*) \cos(\boldsymbol{\Sigma}(\boldsymbol{\mu}^*)) + \mathbf{U}(\boldsymbol{\mu}^*) \sin(\boldsymbol{\Sigma}(\boldsymbol{\mu}^*)). \quad (\text{A17})$$

The special case of two precomputed bases ( $K=2$ ) and one single parameter ( $n_p=1$ ) is extensively described in<sup>20</sup>.

## References

1. Westerhof N, Lankhaar J.-W, Westerhof B. E. The arterial windkessel. *Medical & Biological Engineering & Computing*. 2008;47(2):131–141.
2. Kerckhoffs R. C, et al. Coupling of a 3D finite element model of cardiac ventricular mechanics to lumped systems models of the systemic and pulmonic circulation. *Annals of Biomedical Engineering*. 2007;35(1):1–18.
3. Chabiniok R, et al. Multiphysics and multiscale modelling, data–model fusion and integration of organ physiology in the clinic: ventricular cardiac mechanics. *Interface Focus*. 2016;6(2).
4. Pfäller M. R, et al. The importance of the pericardium for cardiac biomechanics: From physiology to computational modeling. *eprint arXiv:1810.05451*. 2018;.
5. Arts T, Reneman R. S, Veenstra P. C. A model of the mechanics of the left ventricle. *Annals of Biomedical Engineering*. 1979;7(3):299–318.
6. Caruel M, Chabiniok R, Moireau P, Lecarpentier Y, Chapelle D. Dimensional reductions of a cardiac model for effective validation and calibration. *Biomechanics and Modeling in Mechanobiology*. 2014;13(4):897–914.
7. Moulton M. J, Hong B. D, Secomb T. W. Simulation of Left Ventricular Dynamics Using a Low-Order Mathematical Model. *Cardiovascular Engineering and Technology*. 2017;8(4):480–494.
8. Lumens J, Delhaas T, Kirn B, Arts T. Three-Wall Segment (TriSeg) Model Describing Mechanics and Hemodynamics of Ventricular Interaction. *Annals of Biomedical Engineering*. 2009;37(11):2234–2255.
9. Biehler J, Gee M. W, Wall W. A. Towards efficient uncertainty quantification in complex and large-scale biomechanical problems based on a Bayesian multi-fidelity scheme. *Biomechanics and Modeling in Mechanobiology*. 2015;14(3):489–513.
10. Hirschvogel M, Bassilious M, Jagschies L, Wildhirt S, Gee M. A monolithic 3D-0D coupled closed-loop model of the heart and the vascular system: Experiment-based parameter estimation for patient-specific cardiac mechanics. *International Journal for Numerical Methods in Biomedical Engineering*. 2016;33(8):e2842.
11. Gerbeau J.-F, Lombardi D. Approximated Lax pairs for the reduced order integration of nonlinear evolution equations. *Journal of Computational Physics*. 2014;265:246 - 269.
12. Gerbeau J.-F, Lombardi D, Schenone E. Reduced order model in cardiac electrophysiology with approximated Lax pairs. *Advances in Computational Mathematics*. 2015;41(5):1103–1130.
13. Pagani S, Manzoni A, Quarteroni A. Numerical approximation of parametrized problems in cardiac electrophysiology by a local reduced basis method. *Computer Methods in Applied Mechanics and Engineering*. 2018;340:530 - 558.

14. Krysl P, Lall S, Marsden J. E. Dimensional model reduction in non-linear finite element dynamics of solids and structures. *International Journal for Numerical Methods in Engineering*. 2001;51(4):479-504.
15. Milani R, Quarteroni A, Rozza G. Reduced basis method for linear elasticity problems with many parameters. *Computer Methods in Applied Mechanics and Engineering*. 2008;197(51):4812 - 4829.
16. Schilders W. H. A, Lutowska A. A Novel Approach to Model Order Reduction for Coupled Multiphysics Problems:1–49. Cham: Springer International Publishing 2014.
17. Chapelle D, Gariah A, Moireau P, Sainte-Marie J. A Galerkin strategy with Proper Orthogonal Decomposition for parameter-dependent problems—Analysis, assessments and applications to parameter estimation. *ESAIM: Mathematical Modelling and Numerical Analysis*. 2013;47(6):1821–1843.
18. Bonomi D, Manzoni A, Quarteroni A. A matrix DEIM technique for model reduction of nonlinear parametrized problems in cardiac mechanics. *Computer Methods in Applied Mechanics and Engineering*. 2017;324:300–326.
19. Benner P, Gugercin S, Willcox K. A survey of projection-based model reduction methods for parametric dynamical systems. *SIAM Review*. 2015;57(4):483–531.
20. Amsallem D, Farhat C. Interpolation method for adapting reduced-order models and application to aeroelasticity. *AIAA Journal*. 2008;46(7):1803–1813.
21. Farhat C, Chapman T, Avery P. Structure-preserving, stability, and accuracy properties of the energy-conserving sampling and weighting method for the hyper reduction of nonlinear finite element dynamic models. *International Journal for Numerical Methods in Engineering*. 2015;102(5):1077–1110.
22. Sermesant M, et al. Cardiac function estimation from MRI using a heart model and data assimilation: Advances and difficulties. *Medical Image Analysis*. 2006;10(4):642 - 656. Special Issue on Functional Imaging and Modelling of the Heart (FIMH 2005).
23. Chávez C. E, Zemzemi N, Coudière Y, Alonso-Atienza F, Álvarez D. Inverse Problem of Electrocardiography: Estimating the Location of Cardiac Ischemia in a 3D Realistic Geometry. In: Assen H, Bovendeerd P, Delhaas T, eds. *Functional Imaging and Modeling of the Heart*, :393–401Springer International Publishing; 2015; Cham.
24. Finsberg H, et al. Efficient estimation of personalized biventricular mechanical function employing gradient-based optimization. *International Journal for Numerical Methods in Biomedical Engineering*. 2018;34(7):e2982. e2982 cnm.2982.
25. Chabiniok R, et al. Estimation of tissue contractility from cardiac cine-MRI using a biomechanical heart model. *Biomechanics and Modeling in Mechanobiology*. 2012;11(5):609-630.
26. Bertoglio C, Moireau P, Gerbeau J.-F. Sequential parameter estimation for fluid-structure problems: Application to hemodynamics. *International Journal for Numerical Methods in Biomedical Engineering*. 2012;28(4):434–455.
27. Moireau P, et al. Sequential identification of boundary support parameters in a fluid-structure vascular model using patient image data. *Biomechanics and Modeling in Mechanobiology*. 2013;12(3):475-496.
28. Asner L, et al. Estimation of passive and active properties in the human heart using 3D tagged MRI. *Biomechanics and Modeling in Mechanobiology*. 2015;:1-19.
29. Lassila T, Manzoni A, Quarteroni A, Rozza G. A reduced computational and geometrical framework for inverse problems in hemodynamics. *International Journal for Numerical Methods in Biomedical Engineering*. 2013;29(7):741-776.
30. Molléro R, et al. Multifidelity-CMA: a multifidelity approach for efficient personalisation of 3D cardiac electromechanical models. *Biomechanics and Modeling in Mechanobiology*. 2018;17(1):285–300.
31. Newmark N. M. A method of computation for structural dynamics. *Journal of the Engineering Mechanics Division*. 1959;85(3):67–94.

32. Chung J, Hulbert G. A time integration algorithm for structural dynamics with improved numerical dissipation: the generalized- $\alpha$  method. *Journal of Applied Mechanics*. 1993;60(2):371–375.
33. Crank J, Nicolson P. A practical method for numerical evaluation of solutions of partial differential equations of the heat-conduction type. *Mathematical Proceedings of the Cambridge Philosophical Society*. 1947;43(1):50–67.
34. Kunisch K, Volkwein S. Control of the Burgers equation by a reduced-order approach using proper orthogonal decomposition. *Journal of Optimization Theory and Applications*. 1999;102(2):345–371.
35. Chatterjee A. An introduction to the proper orthogonal decomposition. *Current Science*. 2000;:808–817.
36. Kunisch K, Volkwein S. Galerkin proper orthogonal decomposition methods for a general equation in fluid dynamics. *SIAM Journal on Numerical analysis*. 2002;40(2):492–515.
37. Liang Y, et al. Proper orthogonal decomposition and its applications – Part I: Theory. *Journal of Sound and Vibration*. 2002;252(3):527–544.
38. Kerschen G, Golinval J.-C, Vakakis A. F, Bergman L. A. The method of proper orthogonal decomposition for dynamical characterization and order reduction of mechanical systems: an overview. *Nonlinear Dynamics*. 2005;41(1):147–169.
39. Wall W. A, et al. *Baci: a parallel multiphysics simulation environment*. : Technical report, Institute for Computational Mechanics, Technische Universität München; 2018.
40. Heroux M. A, et al. An overview of the Trilinos project. *ACM Transactions on Mathematical Software (TOMS)*. 2005;31(3):397–423.
41. Geuzaine C, Remacle J.-F. Gmsh: A 3-D finite element mesh generator with built-in pre-and post-processing facilities. *International Journal for Numerical Methods in Engineering*. 2009;79(11):1309–1331.
42. Chaturantabut S, Sorensen D. C. Nonlinear model reduction via discrete empirical interpolation. *SIAM Journal on Scientific Computing*. 2010;32(5):2737–2764.
43. Levenberg K. A method for the solution of certain non-linear problems in least squares. *Quarterly of Applied Mathematics*. 1944;2(2):164–168.
44. Marquardt D. W. An algorithm for least-squares estimation of nonlinear parameters. *Journal of the Society for Industrial and Applied Mathematics*. 1963;11(2):431–441.
45. Allemang R. J, Brown D. L. A correlation coefficient for modal vector analysis. *Proceedings of the 1st International Modal Analysis Conference*. 1982;1:110–116.
46. Allemang R. J. The modal assurance criterion—twenty years of use and abuse. *Sound and Vibration*. 2003;37(8):14–23.